INSTITUTE OF PHYSICS PUBLISHING JOURNAL OF OPTICS B: QUANTUM AND SEMICLASSICAL OPTICS

J. Opt. B: Quantum Semiclass. Opt. **5** (2003) R1–R26 PII: S1464-4266(03)53056-7

PhD TUTORIAL

Ultrashort pulse generation by molecular modulation

A V Sokolov[1] **and S E Harris**[2]

[1] Department of Physics and Institute for Quantum Studies, Texas A&M University, College Station, TX 77843-4242, USA
[2] Edward L Ginzton Laboratory, Stanford University, Stanford, CA 94305, USA

E-mail: sokol@physics.tamu.edu

Received 2 September 2002
Published 2 December 2002
Online at stacks.iop.org/JOptB/5/R1

Abstract
This PhD Tutorial describes a new source of coherent radiation, with a spectrum extending over many octaves of optical bandwidth. We demonstrate collinear generation of mutually coherent spectral sidebands, ranging in wavelength from 2.94 μm in the infrared to 195 nm in the ultraviolet. The pulse energies are above 1 mJ/10 ns pulse for each of the nine central sidebands. The essence of our technique is the adiabatic preparation of a macroscopic molecular ensemble in a single vibrational superposition state. When this is achieved, coherent molecular motion modulates laser light and produces a wide frequency modulated (FM)-like spectrum, which allows subfemtosecond pulse compression. We use this source in two experiments: (1) we demonstrate the generation and detection of amplitude and frequency modulated light with a 90 THz modulation frequency; and (2) we demonstrate coherent control of multiphoton ionization on a few-femtosecond timescale, under conditions where photoionization requires eleven photons of the lowest frequency and five photons of the highest frequency of the spectrum. Our experiments demonstrate good mutual coherence of the generated sidebands and suggest a possibility of sub-cycle optical field shaping. This is a first step towards studying subfemtosecond atomic and molecular dynamics.

Keywords: Ultrafast, subfemtosecond, ultrashort pulses, molecular modulation, coherent broadband, Raman generation

(Some figures in this article are in colour only in the electronic version)

1. Introduction

Over the past decade advances in the femtosecond mode-locked laser technology fueled a broad field of ultrafast physics and chemistry [1–3]. This technology allowed time-resolved studies and coherent control of chemical reactions and molecular dynamics [4–8]. Generation of subfemtosecond pulses would extend the horizon of ultrafast measurements to the timescale of electronic motion [9]. This PhD tutorial describes a technique that provides a possibility for such measurements by supplying a source of coherent radiation with the necessary spectral bandwidth [10]. As a first step toward measuring and controlling electronic dynamics, we use this new source to demonstrate coherent control of multiphoton ionization on a few-femtosecond timescale [11].

Short pulse generation requires a wide phase-locked spectrum. Until recently the shortest optical pulses were obtained by expanding the spectrum of a mode-locked laser by self-phase modulation in an optical fibre, and then compensating for group velocity dispersion (GVD) by diffraction grating and prism pairs [12–14]. Continuous

development of this technology resulted in a gradual reduction of pulse duration, from 6 fs in 1987 to 4.4 fs in 2000 [15].

Breaking the 'few-femtosecond barrier' clearly required a new approach. Other authors have discussed generation of subfemtosecond pulses by phase-locking a spectrum of equidistant frequency components:

(1) Hansch has proposed a pulse synthesizer which uses separate phase-locked laser oscillators [16];
(2) workers in the field of high-order harmonic generation (HHG) have predicted the formation of attosecond pulse trains [17–20], and have proposed methods for a single-pulse selection [21, 22];
(3) Imasaka and colleagues have demonstrated the generation of a broad rotational Raman spectrum in molecular hydrogen (H_2) and discussed the possibilities for phase-locking this spectrum [23, 24]; Kaplan and Shkolnikov have predicted the existence of 2π Raman solitons with a phase-locked spectrum that Fourier-transforms into a train of subfemtosecond pulses [25, 26].

There has also been significant work on the dynamics of an intense femtosecond laser pulse in a Raman-active medium, including predictions of 2π pulse formation and attosecond pulse generation [27–29]. In other related work researchers have predicted formation of optical subcycle pulses by coherent propagation effects [30, 31].

The year 2001 saw a breakthrough in ultrashort pulse generation in several directions simultaneously. Impulsive Raman scattering has produced pulses as short as 3.8 fs in the near-ultraviolet [32]. Workers in the field of HHG have measured subfemtosecond pulses in the x-ray spectral region [33–35]. HHG is a unique source of x-ray pulses, but by their very nature these pulses are difficult to control because of intrinsic problems of x-ray optics; besides, the conversion efficiency into these pulses is very low (typically 10^{-5}) [17–22].

We have investigated (theoretically [36–39] and experimentally [10, 40]) a new light source which allows subfemtosecond pulse compression. Our source is based on collinear generation of a wide spectrum of equidistant, mutually coherent Raman sidebands. The essence of our technique is the use of a Raman transition with a sufficiently large coherence that the generation length and the phase-slip length are of the same order. This coherence is established by driving the molecular transition with two single-mode laser fields, slightly detuned from the Raman resonance so as to excite a single molecular superposition state. Molecular motion, in turn, modulates the driving laser frequencies, causing the collinear generation of a very broad FM-like spectrum. In our experiment the spectrum consists of 17 sidebands and extends over many octaves of optical bandwidth (from 2.95 μm in infrared to 195 nm in ultraviolet), with energy above 1 mJ/10 ns pulse for each of the nine central sidebands.

We have used our new light source in two experiments. (1) We have demonstrated the generation and detection of amplitude modulated (AM) and frequency modulated (FM) light with a 90 THz modulation frequency. (2) We have synthesized single-cycle pulses and characterized them by measuring the pulse-shape-dependent multiphoton ionization rate in xenon. Under the conditions of our experiment, photoionization of xenon atoms requires 11 photons of the lowest frequency of the spectrum and 5 photons of the highest frequency.

The applications of our technique are not limited to subfemtosecond pulse generation. One alternative is to use individual sidebands from the generated spectrum as sources of radiation in spectral regions not easily accessible by other techniques. Another possibility is refractive index control in a molecular medium, as proposed by Harris for two sidebands [41], or for a whole comb of frequencies [36, 42].

Our model for the collinear Raman generator is an extension of ideas of electromagnetically induced transparency (EIT) [43, 44] to far-detuned molecular systems. EIT relies on negation of refraction and absorbtion by quantum interference and allows unperturbed propagation of resonant laser beams through optically thick media. Adiabatic preparation of a single coherent superposition state is at the heart of EIT. Applications of EIT include control of refractive index and efficient nonlinear optical conversion in gases (representative papers are cited in [43, 44]; of particular pertinence here, Jain *et al* [45] have demonstrated frequency conversion at maximal atomic coherence). In the past, EIT has only been studied, or experimentally demonstrated, for single-photon detunings which are sufficiently small that the rotating wave approximation applies. Our work on molecular systems may be viewed as broadening the concept of EIT to include an arbitrary number of spectral components, which are spaced by a Raman frequency and far detuned from electronic states.

This PhD tutorial consists of two parts: theoretical (sections 2– 5) and experimental (sections 6– 9). In section 2, we analyse a model molecular system, driven by a set of equidistant frequency sidebands. We show that a beatnote of two laser fields exerts a periodic force, which acts on the nuclei, at the difference frequency of the fields. When tuned close to a Raman resonance, this force results in a well-synchronized molecular oscillation. In essence, all molecules in the medium begin to oscillate in unison with each other, either in phase with the driving force or 180° out of phase, depending on the sign of the detuning from the natural molecular resonance. The molecular motion, in turn, modulates the refractive index, as caused by the electronic transitions, much in the same way as a low-frequency electric field modulates the refractive index of a polar crystal. The modulation of the refractive index leads to the frequency modulation of the driving beatnote, and results in the collinear generation of equidistant frequency sidebands [37]. If dispersion is negligible, the excitation force, which is proportional to the square of the waveform envelope, remains unchanged (in other words, the whole comb of Raman sidebands drives the molecules as efficiently as the initial pair of fields).

In section 3, we show that, in the high-coherence regime, sideband propagation and Raman generation are intrinsically interrelated. During one period of the coherent (well-synchronized) molecular rotation in H_2, the macroscopic refractive index $(n-1)$ of the medium varies by approximately 66%. This variation is not only responsible for the generation of a comb of frequency sidebands, but also determines the change in the average refractive index that each individual sideband sees [36]. This index can be either enhanced or reduced, depending on the phase of molecular oscillations, and

can cause either self-focusing or defocusing. Furthermore, by changing only the sign of the Raman detuning, one should observe a 16-fold reduction (or increase) in the right-angle Rayleigh scatter (which is proportional to $(n-1)^2$).

Section 4 analyses prospects for subfemtosecond pulse compression. We have suggested that the FM waveform, produced by molecular modulation, can be compressed into a train of subfemtosecond pulses by GVD of the same molecular medium [37, 38]. By numerically modeling this process in molecular deuterium (D_2), we calculate a generated train of pulses with a pulse spacing of 11.1 fs and a pulse length of 0.21 fs. Extending these ideas, section 5 shows that molecular modulation can be used to compress mode-locked laser pulses into the subfemtosecond domain [39].

Sections 6–9 describe our experiments, which examine the nature of molecular modulation and explore its possible applications. In section 6 we present results for broadband generation by phased and antiphased molecular states [10]. We use molecular deuterium to demonstrate collinear generation of mutually coherent equidistant sidebands, covering 50 000 cm^{-1} of the spectral bandwidth. We show that, in agreement with theory, generation maximizes at a finite detuning on either side of the Raman resonance, under conditions where the molecular excitation is completely adiabatic.

In section 7 we extend the ideas of molecular modulation and describe an efficient single-sideband converter which is driven by two circularly polarized laser fields [46]. It is well known that a rotating birefringent waveplate will modulate circularly polarized light to produce a single sideband, shifted by twice the rotational frequency of the waveplate. For a diatomic molecule (D_2 in our case) the polarizability depends on the orientation of the molecular axis; thus we can create a rotating waveplate by aligning all the molecules in the D_2 cell and making them rotate in unison. This rotation, in turn, mixes with a third circularly polarized (potentially widely tunable) laser field and generates a single Raman sideband.

Section 8 demonstrates the ability to independently adjust the phases of three sidebands, which are obtained from the broadband collinear Raman generator and spaced by the molecular vibrational frequency, so as to produce AM or FM light [40]. The AM component is detected due to its ability to excite molecular oscillations. We use our AM detection technique to measure the relative phase among Raman sidebands, as a function of the Raman detuning, and observe a π phase shift, which corresponds to the transition from the antiphased to the phased molecular state.

The main implication of the result, described in section 8, is the perfect mutual coherence of the Raman sidebands produced by the molecular modulation. This mutual coherence among the sidebands allows us to recombine them and use spectral modification techniques [47–49] to synthesize any specified femtosecond time structures in a target cell. This is what we do in the experiment described in section 9, where we demonstrate coherent control of multiphoton ionization with shaped few-femtosecond pulses, in a regime not accessible by other sources [11]. Furthermore, we use the multiphoton ionization process to characterize our light source. From indirect measurements we infer the pulse length, produced in our present experiment, to be approximately 2 fs (less than one optical cycle of the applied infrared lasers). The experiment on multiphoton ionization with single-cycle pulses is our first step towards studying atomic dynamics on the timescale of electronic motion.

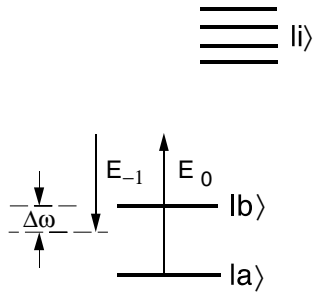

Figure 1. Energy level schematic for establishing coherence ρ_{ab} in a molecular system. Laser fields are applied at the frequencies of the $q = 0$ and -1 sidebands.

2. Molecular modulation: theoretical analysis

In this opening section we describe the theoretical model for the interaction of a molecular system with an arbitrary number of spectral sidebands spaced by (approximately) a Raman frequency. From this model we derive a self-consistent FM solution for the sideband amplitudes. We show that in the limit of small dispersion and limited modulation bandwidth, the sidebands have Bessel-function amplitudes and the molecular motion is unaffected by the generation process.

The coherence ρ_{ab} (figure 1) of the driven molecular transition is central to all work, presented in this PhD tutorial. This coherence is established by driving the molecular transition slightly off resonance (adiabatically) with driving lasers of sufficient intensity that the product of their Rabi frequencies exceeds the product of the detuning from the molecular electronic states and the detuning from the Raman transition. With the linewidth of the applied laser pulses small as compared to the Raman detuning, the magnitude of the molecular coherence approaches 0.5 and its sign is determined by the sign of the Raman detuning.

For the conditions of the previous paragraph, the generation and phase-slip lengths are of the same order, and Raman sideband generation proceeds collinearly and very differently than in the conventional low coherence regime. In essence, the molecular motion now modulates the electronic refractive index much in the same way as a low frequency electric field modulates the refractive index of a polar crystal. Incident optical fields become FM with peak (sinusoidal) frequency deviations and spectral bandwidths that substantially exceed the width of the visible spectrum.

2.1. Summary of the formalism

We start with a summary of the formalism describing the interaction of the multilevel system of figure 1 with a comb of Raman sidebands. This formalism is valid in atomic or molecular systems where the detunings of the laser fields from the electronic states $|i\rangle$ are large compared to the Rabi frequencies and where, therefore, the probability amplitudes of these states are small. We include all possible sidebands,

spaced by the modulation frequency ω_m, regardless of whether the sideband frequencies are applied at the input or are generated as part of the propagation process. We work with the (complex) envelope quantities $E_q(z,t)$ and $\rho_{ab}(z,t)$ for electromagnetic fields and density matrix elements such that the full time and space quantities are

$$\begin{aligned}\hat{E}_q(z,t) &= \mathrm{Re}\{E_q(z,t)\exp[\mathrm{j}(\omega_q t - k_q z)]\},\\ \hat{\rho}_{ab}(z,t) &= \mathrm{Re}\{\rho_{ab}(z,t)\exp[\mathrm{j}(\omega_m t - k_m z)]\},\end{aligned} \tag{1}$$

where

$$\omega_q = \omega_0 + q(\omega_b - \omega_a - \Delta\omega) = \omega_0 + q\omega_m.$$

The modulation frequency ω_m is equal to the difference of the two applied frequencies ω_0 and ω_{-1}. The two-photon detuning $\Delta\omega$ is the difference of ω_m and the Raman transition frequency, and is set by the applied fields. $k_q = \omega_q/c$ and $k_m = \omega_m/c$ are the free-space wavevectors.

We allow for an arbitrary number of virtual states $|i\rangle$ with energies $\hbar\omega_i$. The matrix elements from states $|a\rangle$ and $|b\rangle$ to these states are μ_{ai} and μ_{bi}, respectively. When the derivatives of the probability amplitudes of the upper states $|i\rangle$ are small compared to the detunings from these states, the problem can be written in terms of an effective 2×2 Hamiltonian [36, 41]:

$$H_{eff} = -\frac{\hbar}{2}\begin{bmatrix}\sum_q a_q|E_q|^2 & \sum_q b_q E_q E_{q-1}^*\\ \sum_q b_{q+1}^* E_q E_{q+1}^* & \sum_q d_q|E_q|^2 - 2\Delta\omega\end{bmatrix} \tag{2}$$

$$\equiv -\frac{\hbar}{2}\begin{bmatrix}A & B\\ B^* & D - 2\Delta\omega\end{bmatrix}. \tag{3}$$

A detailed derivation of this Hamiltonian is given in appendix A of a recent paper [50]. All rotating and non-rotating, as well as cross-transition, terms are retained within this effective Hamiltonian. The constants a_q, b_q and d_q determine dispersion and coupling and are

$$\begin{aligned}a_q &= \frac{1}{2\hbar^2}\sum_i\left[\frac{|\mu_{ai}|^2}{(\omega_i-\omega_a)-\omega_q} + \frac{|\mu_{ai}|^2}{(\omega_i-\omega_a)+\omega_q}\right],\\ b_q &= \frac{1}{2\hbar^2}\sum_i\left[\frac{\mu_{ai}\mu_{bi}^*}{(\omega_i-\omega_a)-\omega_q} + \frac{\mu_{ai}\mu_{bi}^*}{(\omega_i-\omega_b)+\omega_q}\right],\\ d_q &= \frac{1}{2\hbar^2}\sum_i\left[\frac{|\mu_{bi}|^2}{(\omega_i-\omega_b)-\omega_q} + \frac{|\mu_{bi}|^2}{(\omega_i-\omega_b)+\omega_q}\right].\end{aligned} \tag{4}$$

We assume that all the molecular population is initially in the ground state. We also assume the ideal case of zero linewidth for the $|a\rangle$–$|b\rangle$ transition.

Terms A and D are proportional to the field intensities and represent (doubled) Stark shifts of the molecular levels. The quantity B represents a driving force (Raman–Rabi frequency), which excites the molecular oscillation at the frequency ω_m. This force is proportional to the near-resonant Fourier component (at ω_m) of the laser intensity envelope.

The propagation equation for each laser field is obtained within the slowly-varying-envelope approximation (SVEA), which requires that the envelope function of the electric field not vary significantly over either one temporal optical cycle or one wavelength. The general form of this SVEA equation is

$$\left(\frac{\partial}{\partial z} + \frac{\mathrm{j}}{2k}\nabla^2 + \frac{1}{c}\frac{\partial}{\partial t}\right)E_\omega = -\frac{\mathrm{j}}{2}\eta\omega P_\omega, \tag{5}$$

where η is the impedance of free space $\eta = (\mu/\epsilon_0)^{1/2} = 1/\epsilon_0 c$, $k = 2\pi/\lambda$ is the optical (free-space) wavevector and beam diffraction is allowed for by $\nabla^2 = (\partial^2/\partial x^2) + (\partial^2/\partial y^2)$. The spatio-temporal evolution of the electric field envelope of the spectral component with frequency ω is driven by the macroscopic polarization P_ω of the medium.

For our system, with the assumption of negligible diffraction, the propagation equation for the qth Raman sideband, in a time frame moving with a speed of light c, is

$$\begin{aligned}\frac{\partial E_q}{\partial z} = -\mathrm{j}\eta\hbar\omega_q N(&a_q\rho_{aa}E_q + d_q\rho_{bb}E_q\\ &+ b_q^*\rho_{ab}E_{q-1} + b_{q+1}\rho_{ab}^*E_{q+1}).\end{aligned} \tag{6}$$

A detailed derivation of this propagation equation is given in appendix B of a recent paper [50]. The quantities ρ_{ij} are the elements of the 2×2 density matrix. N is the number of molecules per volume. The refractive index of the qth mode, if alone with all molecules in state $|a\rangle$, is $n_q = 1 + (N\hbar a_q/\epsilon_0)$, and with all molecules in state $|b\rangle$ is $1 + (N\hbar d_q/\epsilon_0)$.

From equations (2) and (6) we obtain conservation relations for the total power and the number of photons [36]:

$$\frac{\partial}{\partial z}\left(\sum_q \frac{|E_q|^2}{2\eta}\right) = -\frac{N\hbar}{2}(\omega_b-\omega_a)\left[\frac{\partial}{\partial t}(\rho_{bb}-\rho_{aa})\right], \tag{7}$$

$$\frac{\partial}{\partial z}\left(\sum_q \frac{1}{\hbar\omega_q}\frac{|E_q|^2}{2\eta}\right) = 0. \tag{8}$$

These conservation relations are very intuitive: first of all, the energy of a closed system (laser fields + molecules) must be conserved. Second, in a Raman system photons are emitted and absorbed in pairs, such that for every photon absorbed there is a photon emitted. Even in the presence of a changing atomic population, the total number of photons remains constant with distance.

2.2. Preparation of molecular eigenstates

The 2×2 Hamiltonian allows understanding of the time evolution of a Raman system by analogy with a two-level system [51]. A Raman system can follow a single eigenstate if it is excited adiabatically, or exhibit Raman–Rabi-flopping when the excitation is turned on abruptly. We will concentrate on adiabatic Raman evolution which relates our work to EIT.

There is a large literature on EIT in its own right and on its relation to lasers without population inversion. Representative papers are cited in [43, 44, 52–57]. Of immediate pertinence, Gaubatz *et al* [58] have studied population trapping and adiabatic preparation in molecules. Earlier, Grischkowsky *et al* [59–61] and Oreg *et al* [62] had described adiabatic preparation in two-state and multi-state systems. Our work is also related to the work of Kaplan and Shkolnikov on Raman solitons [25, 26]. These authors have shown that a spectrum of Raman modes of intensity sufficient to form a (Raman) 2π pulse would propagate without variation in area. The essential difference of their work from ours is the same as that of self-induced transparency from EIT: the former depends on pulse area and the latter does not.

In common with other types of EIT and population trapping, we must choose an eigenstate of the effective

Hamiltonian which evolves smoothly from the ground state $|a\rangle$. Defining

$$B = |B|\exp(\mathrm{j}\varphi); \qquad \tan\theta = \frac{2|B|}{2\Delta\omega - D + A}, \tag{9}$$

this eigenstate and the difference of the eigenvalues of the Hamiltonian are

$$|+\rangle = \cos\frac{\theta}{2}\exp\left(\mathrm{j}\frac{\varphi}{2}\right)|a\rangle + \sin\frac{\theta}{2}\exp\left(-\mathrm{j}\frac{\varphi}{2}\right)|b\rangle, \tag{10}$$

$$E_+ - E_- = \sqrt{\left(\Delta\omega - \frac{D}{2} + \frac{A}{2}\right)^2 + |B|^2}. \tag{11}$$

The phased or anti-phased state is selected by the sign of the two-photon detuning. The coherence ρ_{ab} is then

$$\rho_{ab} = \tfrac{1}{2}\sin\theta\exp(\mathrm{j}\varphi). \tag{12}$$

For molecular systems with large detunings, the Stark shifts $A/2$ and $D/2$ are approximately equal and $\theta \cong \tan^{-1}(2|B|/2\Delta\omega)$. One method of achieving the condition $\rho_{ab} = -0.5$ at $z = 0$ is to choose $\Delta\omega$ negative and to increase the product of the two incident fields until θ is near 90°. This is done adiabatically with the product of the fields changing slowly as compared to the separation of the eigenvalues. Alternatively, at a fixed field strength, one may allow $\Delta\omega$ to chirp from an initial negative value toward zero.

2.3. Self-consistent FM solution

We now examine the analytically solvable case of negligible dispersion and limited modulation bandwidth. We take all of the sidebands to be sufficiently far from the resonances that, in equation (4), $a_q = d_q \equiv a_0$ and $b_q \equiv b_0$. We define propagation constants $\beta_q = \eta\hbar\omega_q N a_0$ and change variables by $E_q = \tilde{E}_q\exp(-\mathrm{j}\beta_q z)$, $\rho_{ab} = \tilde{\rho}_{ab}\exp(-\mathrm{j}\beta_m z)$. With these approximations and definitions, equation (6) becomes

$$\frac{\partial\tilde{E}_q}{\partial z} = -\mathrm{j}\frac{b_0}{a_0}\beta_q(\tilde{\rho}_{ab}\tilde{E}_{q-1} + \tilde{\rho}^*_{ab}\tilde{E}_{q+1}). \tag{13}$$

The quantity $\tilde{\rho}_{ab} = \frac{1}{2}\sin\tilde{\theta}\exp(\mathrm{j}\tilde{\varphi})$, where $\tilde{\theta}$ and $\tilde{\varphi}$ are given by equation (9) with E_q replaced by $\tilde{E}_q$. As the boundary conditions for the propagation equation we assume that the fields $E_0(0)$ and $E_{-1}(0)$ are applied at the input of the medium and all other Raman sidebands are generated in the medium.

We assume a restricted modulation bandwidth such that all ω_q are equal to ω_0 and $\beta_q \equiv \beta_0 \equiv \beta$. By using the Bessel function identities

$$\frac{\partial J_n(x)}{\partial x} = \frac{1}{2}[J_{n-1}(x) - J_{n+1}(x)], \tag{14}$$

$$\sum_{n=-\infty}^{+\infty} J_{n+q}(x)J_{n+p}(x) = \delta_{pq}, \tag{15}$$

it may be verified that, with $\gamma = \frac{b_0}{a_0}\beta_0\sin[\theta(0)]$, the solution [37]

$$\begin{aligned}
&\tilde{\varphi}(z) = \varphi(0) = \arg[E_0(0)E^*_{-1}(0)],\\
&\tilde{\rho}_{ab}(z) = \rho_{ab}(0) = \tfrac{1}{2}\sin[\theta(0)]\exp[\mathrm{j}\varphi(0)],\\
&\tilde{E}_q(z) = E_0(0)\exp\left[\mathrm{j}\left(\varphi(0) - \frac{\pi}{2}\right)q\right]J_q(\gamma z)\\
&\quad + E_{-1}(0)\exp\left[\mathrm{j}\left(\varphi(0) - \frac{\pi}{2}\right)(q+1)\right]J_{q+1}(\gamma z),
\end{aligned} \tag{16, 17}$$

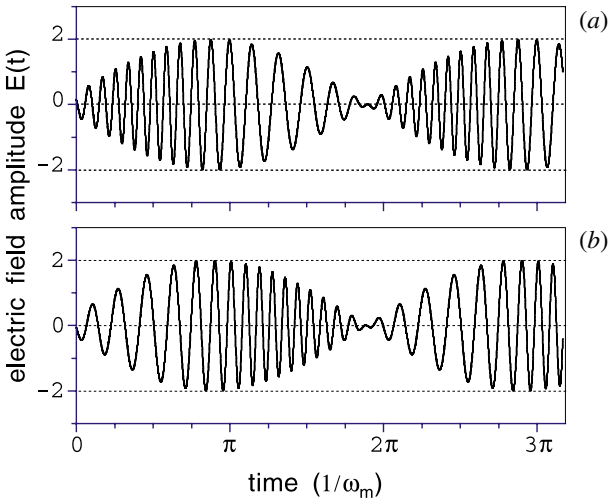

Figure 2. Normalized electric field amplitude versus time at the output of an (*a*) antiphased and (*b*) phased dispersion-free medium. The parameters are: $E_0(0) = 1$, $E_{-1}(0) = 1$ and $\omega_0/\omega_m = 18$. The length of the medium is such that $\gamma L = 7$. Time is measured in units of $1/\omega_m$.

satisfies both density matrix and propagation equations and also the boundary condition at $z = 0$. [Note that $E_q(0) = \tilde{E}_q(0)$.] It is important that the generation process preserves the driving force B and leaves the eigenvectors of the Hamiltonian unchanged. We use equation (17) and the identity

$$\sum_{n=-\infty}^{+\infty} J_n(x)\exp(\mathrm{j}n\omega t) = \exp[\mathrm{j}x\sin(\omega t)], \tag{18}$$

to construct the time domain signal (figure 2):

$$\begin{aligned}
E(t) = \mathrm{Re}\{&E_0(0)\exp\mathrm{j}[\omega_0 t + \gamma z\cos(\omega_m t + \varphi(0))]\\
&+ E_{-1}(0)\exp\mathrm{j}[\omega_{-1}t + \gamma z\cos(\omega_m t + \varphi(0))]\}.
\end{aligned} \tag{19}$$

Equation (19) is a superposition of two FM signals with centre frequencies corresponding to the frequencies which are applied at $z = 0$ and a peak phase deviation γz.

The total number of sidebands generated in a cell of length L is approximately equal to $2\gamma L$. The assumption of limited modulation bandwidth ($\omega_q = \omega_0$) implies that $\gamma z \ll \omega_0/\omega_m$, i.e. the peak frequency excursion must be small compared to the centre frequency. We have checked that, when this assumption is satisfied, the solution of equation (17) coincides with the exact numerical solution of equation (13).

The solution of equations (16) and (17) applies to either the antiphased state ($\sin\theta < 0$) or the phased state ($\sin\theta > 0$). Figure 2 shows the time domain signals for each case; both are FM signals with an envelope at the beat frequency ω_m. But, in the antiphased case (figure 2(*a*)), the higher frequencies (blue) are temporally advanced with regard to the lower frequencies (red), while, in the phased case (figure 2(*b*)), red is advanced as compared to blue. Note that in both cases the envelope of the beatnote is preserved and, as a result, the driving force, which acts on the molecules, is unchanged. This is what makes the FM solution consistent with both density matrix and propagation equations.

Maxwell equations allow analytical solutions for modulation and compression of light pulses with unlimited

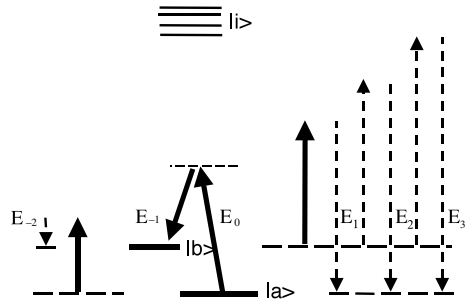

Figure 3. Energy level diagram for Raman generation in a highly coherent molecular medium. Solid arrows represent the applied fields and broken arrows show the generated sidebands.

bandwidth, which propagate in a dispersionless medium with a prepared polarization. However, these non-self-consistent solutions only apply to media with predetermined molecular oscillations, either sinusoidal [50, 63, 64] or non-sinusoidal [65, 66].

We note that there is a relationship of our work to the suggestion (by Kocharovskaya *et al* [67]) to use a Raman medium inside a laser cavity, so as to provide phase modulation to cause mode locking. We would also like to mention that the formalism, presented in this section and in the next two sections, was reproduced and analysed in detail by Kien *et al* [50, 68].

3. Refractive index of a strongly driven Raman medium

We have shown that coherent molecular motion can modulate light and produce a wide spectrum of collinear sidebands. In this section we analyse the implications of this result with regard to the possibility of refractive index control.

The process of molecular modulation significantly affects the propagation of individual sidebands. The large variation of the refractive index is not only responsible for the sideband generation, but also causes the enhancement or reduction (depending on the phase of molecular oscillations) in the refractive index that each individual spectral sideband sees.

From the frequency domain viewpoint, as shown in figure 3, the applied laser fields (solid arrows) and the generated Raman sidebands (broken arrows) form a multiple Λ scheme and interact with molecules in an EIT-like manner. Depending on the sign of the Raman detuning, the refractive index, seen by the sidebands, is either enhanced or reduced.

3.1. Phase retardation of Raman sidebands

The approximate Bessel-function solution for the sideband amplitudes (equation (17) of section 2) allows us to derive an analytical expression for the phases of the centre (low-order) sidebands. Using the asymptotic form for the Bessel functions

$$J_q(\gamma z) \approx \sqrt{2/(\pi\gamma z)}\cos\left[\gamma z - \left(q+\frac{1}{2}\right)\frac{\pi}{2}\right], \qquad (20)$$

which is valid for $|\gamma z| \gg q(q+1)/2$, we find the phase of an individual sideband (compared to the vacuum propagation phase):

$$\arg[E_q(z)] = C(q) - (\beta+\gamma)z + s(z), \qquad (21)$$

where $C(q) = \arg[E_0(0)] + \frac{\pi}{4} + \varphi(0)q$. $s(z)$ is a periodic function of distance such that $|s(z)| \leqslant \frac{\pi}{2}|\frac{|E_0(0)|-|E_{-1}(0)|}{|E_0(0)|+|E_{-1}(0)|}|$ and $s(z) \equiv 0$ for $|E_0(0)| = |E_{-1}(0)|$. The propagation and generation constants $\beta \equiv \beta_0 = \eta\hbar\omega_0 N a_0$ and $\gamma = \frac{b_0}{a_0}\beta_0 \sin[\theta(0)]$ are the same as defined in section 2. Note that γ is negative for the antiphased state and positive for the phased state of the molecular system.

We compare this result with the exact numerical solution of equations (6) and (12) for molecular hydrogen (H_2) ($\omega_b - \omega_a = 354$ cm^{-1} is the fundamental rotational transition in H_2). We take all molecules in the $J = 0$ ground state. The constants a_q, b_q and d_q include the contributions of all allowed rotation–vibrational transitions in Lyman and Werner bands. Matrix elements are obtained from Allison and Dalgarno [69] and transition frequencies from Herzberg [70]. We assume monochromatic fields E_0 and E_{-1} to be applied at $z = 0$, with power densities of 10^{10} W cm^{-2}, and frequencies $\omega_{-1} = 25\,189$ cm^{-1} and $\omega_0 = 25,543$ cm^{-1} (frequency-doubled Ti:sapphire). The two-photon detuning is $\Delta\omega = \pm 0.5$ GHz. For $N = 2.69 \times 10^{19}$ molecules cm^{-3} (corresponding to 1 atm cell pressure at room temperature) we calculate $\sin\theta = \pm 0.97$; $\gamma = \pm 8.42$ rad cm^{-1}; $\beta = 13.02$ rad cm^{-1}.

Figure 4 shows sideband phases versus distance as predicted by equation (21). In all plots full lines represent the sidebands generated by the antiphased state, broken lines represent generation by the phased state and dotted lines show, for comparison, the phase accumulation of a single sideband if propagating alone. Data points (circles for the antiphased and crosses for the phased state) show results of the numerical simulation described in the previous paragraph. We observe good agreement between analytical and numerical results. The deviation at longer distances occurs when the limited bandwidth assumption is violated (a comb of around 170 sidebands, covering 60 000 cm^{-1} of the spectrum, is generated at $\beta z = 97$ rad, which corresponds to a 7.5 cm-long cell at $N = 2.69 \times 10^{19}$ molecules cm^{-3}).

3.2. Analytical expression for the refractive index

Using equation (21), in the case of $|E_0(0)| \approx |E_{-1}(0)|$, the refractive index for each sideband is found as

$$n = 1 - \frac{\mathrm{d}}{\mathrm{d}z}\arg[E_q(z)]\frac{\lambda_0}{2\pi} = 1 + (\beta+\gamma)\frac{\lambda_0}{2\pi}, \qquad (22)$$

where λ_0 is a centre wavelength of the generated spectrum. The quantity $n_0 = 1 + \beta\lambda_0/(2\pi)$ is the refractive index for a monochromatic field.

For the numerical simulation of figure 4, the refractive index (relative to vacuum) for centre sidebands is reduced by almost a factor of four for the antiphased molecular state when compared to the phased molecular state. This difference should be readily observable experimentally. By changing only the sign of the Raman detuning one should observe a 16-fold reduction (or increase) in the right-angle Rayleigh scatter (proportional to $(n-1)^2$). Note that when $\gamma = -\beta$ ($b_0 = a_0$; $\sin\theta = -1$, which occurs in the antiphased state at maximal coherence) the refractive index for the centre sidebands is unity (as predicted in [36]).

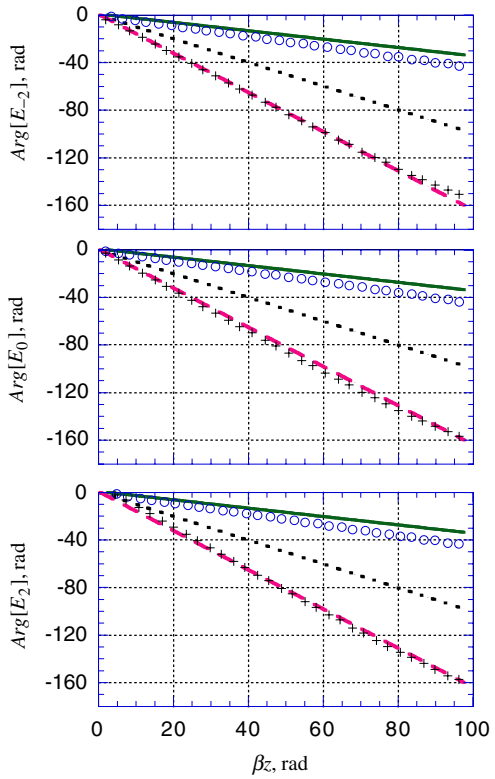

Figure 4. Raman sideband phases as generated in a 7.5 cm-long H_2 cell at 1 atm, with two applied fields of 10^{10} W cm^{-2}. Analytical results are shown by full lines (for the antiphased state) and broken lines (for the phased state). Data points (circles for the antiphased and crosses for the phased state) represent numerical results. Dotted lines show the phase accumulation of a single sideband if propagating alone.

3.3. Raman self-focusing and defocusing

The change in the refractive index due to the field–molecule interaction causes self-focusing of the laser beams (for the phased state of the medium) or self-defocusing (for the antiphased state). If we assume that the coherence of the medium varies smoothly across the transverse beam profile, from its maximum value in the centre to a zero in the wings of the beam, the focal distance is

$$f_R = \frac{r_0^2}{(n-n_0)L} = \frac{2\pi r_0^2}{\lambda_0 \gamma L}, \tag{23}$$

where r_0 is the radius of the laser beam and γ is the generation constant on the axis of propagation. We have assumed the interaction length $L \ll f_R$ and neglected beam diffraction. Note that the wavefront perturbation due to the nonlinear refractive index is directly proportional and the focal distance is inversely proportional to the number of Raman sidebands generated. If $2|\gamma|L = 180$ sidebands, $r_0 = 1$ mm, $\lambda_0 = 400$ nm, then $|f_R| = 17.5$ cm.

If it is desired that the Raman sideband generation is unaffected by the self-focusing (or defocusing), the cell length L should be made shorter than f_R. This constraint can be overcome by increasing the applied laser intensities and making the nonlinear response of the medium close to its maximum value ($|\rho_{ab}| \approx 0.5$) for most of the transverse beam profile. The variation in the refractive index for the central part of the beam will then be reduced.

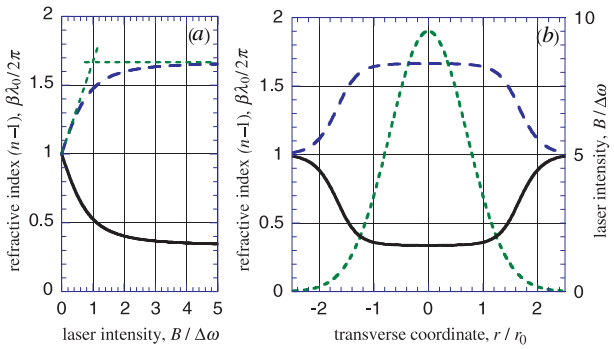

Figure 5. Refractive index for centre sidebands as a function of (*a*) the applied laser intensity and (*b*) the transverse coordinate of the laser beam. Broken curves correspond to the phased, and full curves to the antiphased, state of the Raman medium. Part (*b*) also shows the assumed Gaussian beam profile (dotted curve).

Figure 5(a) shows the refractive index for the centre sidebands, calculated by equation (22) for H_2 (full curve for the antiphased state and broken curve for the phased state) as a function of the ratio of two-photon Rabi frequency to Raman detuning ($B/\Delta\omega$). The refractive index first changes linearly with the driving intensity and then, at high enough intensities, approaches its limiting value $n = 1 + \frac{\beta\lambda_0}{2\pi}(1 \pm \frac{b_0}{a_0})$. Figure 5(*b*) shows the refractive index profile across a Gaussian beam with the centre intensity such that $B/\Delta\omega = 9.5$. The profile is far from spherical and the definition of the focusing distance is ambiguous, but clearly it is flat for most of the beam and self-focusing is reduced. For the case of equal input intensities of 10^{10} W cm^{-2}, the two-photon Rabi frequency is $B = 2.02$ GHz.

The derived expression for the refractive index is only valid for the low-order sidebands of a broad Raman spectrum, generated collinearly in a short low-pressure cell at high coherence. If the cell length becomes larger than the calculated self-focusing (or defocusing) distance, then the beam propagation becomes more complicated because low- and high-order Raman sidebands propagate at different angles. Diffraction was left out from our formalism and can be included to the extent that the beam propagation within the molecular medium is near parallel.

4. Subfemtosecond pulse compression

In this section we show that molecular modulation, produced by the antiphased state, can result in subfemtosecond pulse compression. The idea is very simple: the FM beatnote of figure 2 looks like a train of chirped pulses. In particular, in figure 2(a) the chirp is negative and thus can be compensated by propagation through a certain length of a medium with normal GVD.

The same molecular medium, which provides the frequency modulation, possesses the necessary dispersion. Moreover, it turns out that the frequency modulation and pulse compression can occur concurrently in a single-component molecular gas. We model this process numerically for H_2 and D_2. We observe that, as the modulation spectrum grows in the

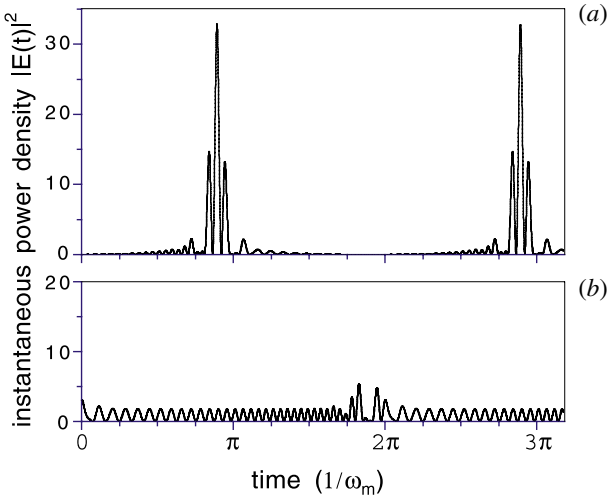

Figure 6. Normalized instantaneous power density versus time for the signals of figure 2 after transmission through a medium with a frequency-invariant GVD and a length determined by equation (24).

frequency domain, the pulses compress in the time domain, down to 0.21 fs at the output of the medium.

4.1. Pulse compression by linear GVD

We analyse the waveforms of figure 2; both are FM signals with an envelope at the beat frequency ω_m. But, in the antiphased case (figure 2(*a*)), the higher frequencies (blue) are temporally advanced with regard to the lower frequencies (red) while, in the phased case (figure 2(*b*)), red is advanced as compared to blue. This difference is important: when $E_0(0) \sim E_{-1}(0)$, only the signal generated by the antiphased state allows pulse compression in a normally dispersive medium.

This compression is obtained by setting the group velocity delay which corresponds to the frequency deviation $\omega_d = \omega_m \gamma L$ equal to $\pi/(2\omega_m)$. Here, but not in the numerical work which follows, we assume a frequency invariant GVD $\partial^2 k/\partial\omega^2$. The medium length l which is necessary for pulse compression is then determined by [37]

$$\left.\frac{\partial^2 k}{\partial \omega^2}\right|_{\omega=\omega_0} l = \frac{\pi}{2\omega_m^2 \gamma L}. \tag{24}$$

Figure 6(a) shows the (squared) signal which is obtained when that of figure 2(a) is transmitted through a medium of this length. Pulse compression with a ratio of pulse width to pulse separation of about $1/(2\gamma L)$ is observed. Figure 6(b) shows the result of transmitting the signal, as driven by the phased state (figure 2(b)), through this same medium.

4.2. Concurrent frequency modulation and pulse compression

We turn next to the numerical solution for D_2 [37]. We do not make any of the dispersive approximations described above, but rather calculate the refractive index for each frequency exactly. We find that both generation and pulse compression may be accomplished concurrently in the same medium. We assume E_0 and E_{-1} to be applied at $z = 0$ and retain sidebands between $q = -9$ and 18. The solution of equation (6) is obtained by forward stepping from $z = 0$ with the density matrix elements recalculated at each step.

We consider the fundamental vibrational transition in D_2 with $\omega_m = 2994$ cm^{-1} and take all molecules in the $J = 0$ ground state. Table 1 gives numerical values for the constants a_q, b_q and d_q (in MKS units), calculated from equation (4). These constants include the contributions of the first 53 vibrational transitions of the Lyman band and the first 19 transitions of the Werner band. Oscillator strengths and Franck–Condon factors are obtained from Allison and Dalgarno [69] and energies are obtained from Herzberg [70]. The D_2 density and the total cell length are chosen such that the zeroth sideband, if propagating alone, would accumulate a phase shift $\beta_0 L = 14\pi$ rad. At a pressure of 1 atm, this corresponds to $L = 3.6$ cm.

We envision using single-mode pulsed lasers with pulse lengths of ∼5 ns and pulse energies of ∼50 mJ. We take the applied laser frequencies to be $\omega_0 = 28\,183$ cm^{-1} (frequency-tripled Nd:YAG) and $\omega_{-1} = 25\,189$ cm^{-1} (frequency-doubled Ti:sapphire). We choose the Raman detuning $\Delta\omega = -1$ GHz to be much larger than both the Raman linewidth (∼0.3 GHz for D_2 at STP) and the laser linewidth (∼0.1 GHz for a single-mode, 5 ns pulse laser). We set the power densities of E_0 and E_{-1} at $z = 0$–10^{11} W cm^{-2}. Evaluating equation (9), $\sin\theta(0) \approx -0.9$. The coherence $|\rho_{ab}| \approx 0.45$ and the cell length are set such that about twenty sidebands are generated and the concurrent group velocity delay is correct for pulse compression.

Figure 7 shows spectral and temporal evolution as a function of distance for the conditions of the previous paragraph. Sideband frequencies are predicted to range from about 1.4 μm in the infrared to 150 nm in the vacuum ultraviolet. At the appropriate cell length these frequencies synthesize a train of pulses with a pulse separation of 11.1 fs and a pulse length of 0.21 fs. (Similar results for vibrations in H_2 are given in [68].) We find sharp pulse compression at experimental conditions which are readily realizable.

Because the ratio of the applied optical frequencies to the Raman transition frequency is, in general, non-integer, the peak of the optical cycle will drift from pulse to pulse within a narrow envelope. This envelope (width = 0.72 fs) is shown by the broken curve in each of the time domain plots of figure 7. If one allows for independent tuning and phase-locking of the two driving frequencies, one may be able to control the phase of optical cycles under the envelope.

4.3. Rotational versus vibrational modulation

The extension of the above ideas to the rotational, as compared to the vibrational, molecular spectrum has three significant advantages. These are:

(1) the ratio of the molecular coupling constant to the molecular dispersion is several times larger;
(2) the repetition rate of the periodic pulse train is an order of magnitude smaller, promising a possibility for single-pulse selection; and
(3) the use of rotational Raman scattering allows a much larger number of sidebands to be generated at the same driving laser intensities, with a total spectral width as large as in the vibrational case.

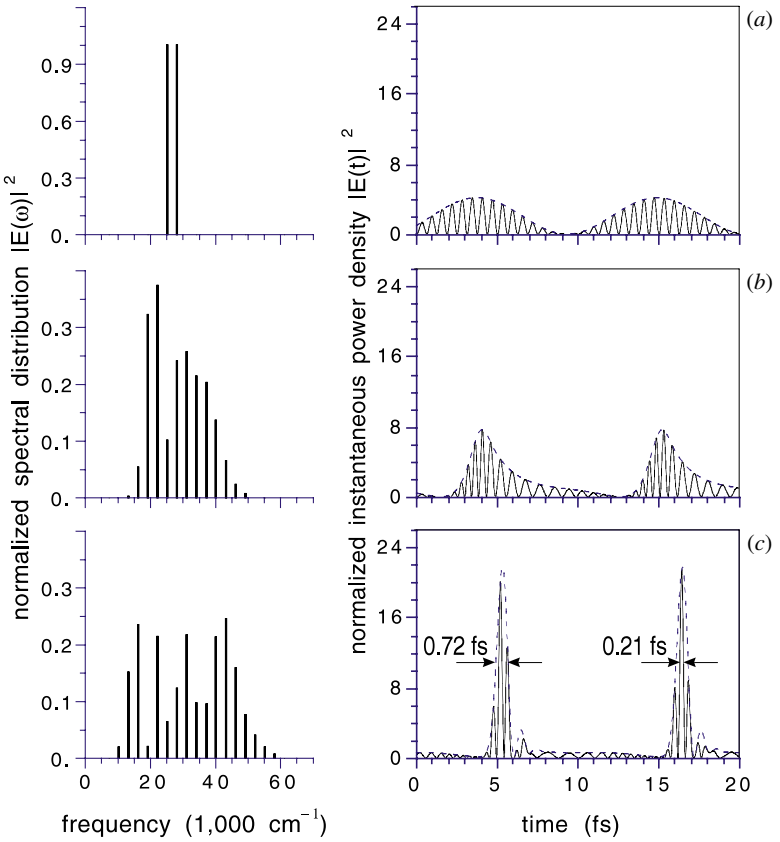

Figure 7. Frequency spectrum (left) and instantaneous power density versus time (right) in D_2 at 1 atm pressure with applied power densities at $z = 0$ such that $\rho_{ab} = -0.45$. Parts (*a*)–(*c*) show the spectrum and temporal waveform for (*a*) $z = 0$ cm, (*b*) $z = 1.8$ cm, (*c*) $z = 3.6$ cm. Sideband powers are normalized to those of the incident fields. The broken curves on the time domain plots show the envelopes of possible single-cycle pulses (reprinted from [37]).

Table 1. Dispersion and coupling constants for the fundamental vibrational transition in D_2, in MKS units, for frequencies such that the $q = 0$ sideband corresponds to a wavelength of 807 nm (each entry is to be multiplied by 2.349×10^{-7}).

q	−4	−3	−2	−1	0	1	2	3	4
a_q	0.986	0.987	0.989	0.994	1.000	1.008	1.018	1.030	1.044
d_q	1.047	1.048	1.051	1.056	1.064	1.073	1.084	1.098	1.114
b_q	0.188	0.188	0.189	0.190	0.191	0.193	0.196	0.199	0.203

We perform a numerical simulation (similar to the one described in the previous subsection) for molecular rotations in H_2 [38]. We show concurrent Raman generation and pulse compression. We assume monochromatic fields E_0 and E_{-1} to be applied at $z = 0$, with power densities of 10^{10} W cm^{-2}, and retain sidebands between $q = -80$ and 160. The solution of equation (6) is obtained by forward stepping from $z = 0$ with the density matrix elements recalculated at each step.

We consider the fundamental rotational transition in H_2 with $\omega_b - \omega_a = 354$ cm^{-1} and take all molecules in the $J = 0$ ground state. The constants a_q, b_q and d_q include the contributions of all allowed rotation–vibrational transitions in Lyman and Werner bands. Transition frequencies are obtained from Herzberg [70]. The applied laser frequencies are $\omega_{-1} = 25\,200$ cm^{-1} and $\omega_0 = 25\,554$ cm^{-1} (frequency-doubled Ti:sapphire) and the two-photon detuning is $\Delta\omega = -0.5$ GHz. The calculated detunings from all other Raman resonances in H_2 are much larger and we neglect the excitation of these transitions.

Reduced matrix elements of the dipole moment operator P are related to vibrational band Einstein-A coefficients:

$$|\langle J'', \upsilon''||P||J', \upsilon'\rangle|^2 = \frac{3}{8\pi^2}\varepsilon_0\hbar\lambda_i^3 H_{J''J'}A_{\upsilon'\upsilon''}, \qquad (25)$$

where λ_i is the transition wavelength. The Honl–London factors $H_{J''J'}$ for P, Q, and R branches are J'', 0 and $J''+1$ for the Lyman band, and $J''-1$, $2J''+1$ and $J''+2$ for the Werner band, respectively. The coefficients $A_{\upsilon'\upsilon''}$ for the Lyman and Werner electronic bands of H_2 are obtained from Allison and Dalgarno [69]. We calculate the matrix elements μ_{ai} and μ_{bi} (for light of a particular polarization) by multiplying $\langle J'', \upsilon''||P||J', \upsilon'\rangle$ by appropriate $3j$-symbols (we assume linearly polarized fields).

As shown in equation (4), dispersion constants a_q and d_q consist of sums over positive terms proportional to $|\mu_{ai}|^2$ and $|\mu_{bi}|^2$. However, coupling constants b_q involve terms proportional to cross-products $\mu_{ai}\mu_{bi}^*$, which can be positive or negative and can partially cancel each other. This partial

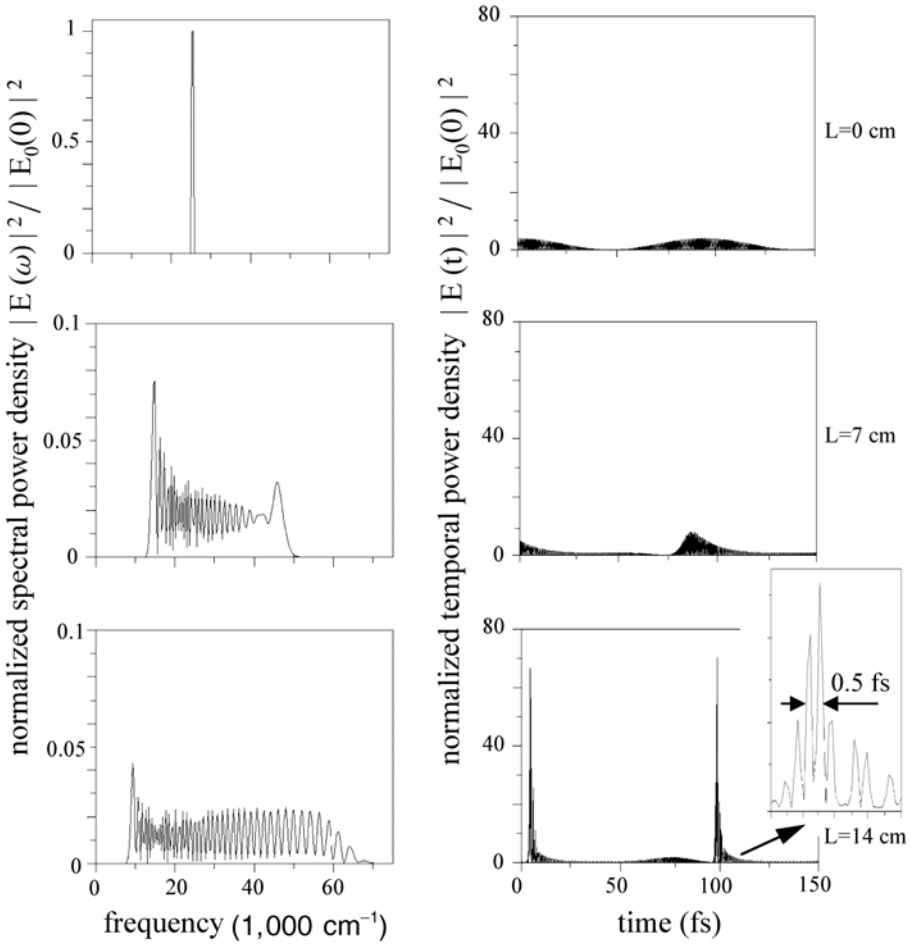

Figure 8. Evolution of the ultrashort pulses in the time domain (right) and frequency domain (left) through the 14 cm-long hydrogen cell at 1 atm pressure. The applied laser power densities are 10^{10} W cm^{-2}, such that $\rho_{ab} = -0.45$. Sideband powers are normalized to those of the incident fields (reprinted from [38] with permission of OSA).

cancellation and reduction of Raman polarizabilities occur if $|a\rangle$ and $|b\rangle$ belong to different vibrational levels; in that case it is important to keep track of relative signs of vibrational wavefunction overlap integrals (squares of which give Frank–Condon factors). In the case of rotational Raman scattering such cancellations do not occur, allowing for higher coupling constants. It is interesting to note that the ratio between the rotational and the vibrational Raman polarizabilities is roughly equal to the ratio of the internuclear distance to the peak-to-peak amplitude of molecular vibrations at $|\rho_{ab}| = 0.5$.

Figure 8 shows the numerically calculated spectral and temporal profiles of the generated waveform at different distances in the H_2 cell at 1 atm pressure. At $z = 14$ cm there are nearly 180 sidebands generated that cover 70 000 cm^{-1} of the spectrum and Fourier transform into a train of pulses with 0.5 fs pulse width and 94 fs pulse spacing, and with the peak intensity exceeding the average intensity by a factor of 35. We note that the coherence $\rho_{ab} = -0.45$ stays roughly the same (both in magnitude and in phase) through the medium.

The pulse compression of figure 8 is not perfect. We note that the phases of sidebands are well determined, though not equal, and suggest that they can be compensated almost perfectly using, for instance, spectral filtering with a phase mask [47–49]. Figure 9 shows the temporal waveform of a signal with the spectral power densities of figure 8 (generated in a 14 cm-long H_2 cell at 1 atm) and phases perfectly corrected by an external spectral-phase filter. We predict half-cycle pulses (duration 0.22 fs) with a peak intensity exceeding the total input intensity by a factor of 140.

We have examined the sensitivity of this technique to fluctuations of applied intensities, cell pressure and length. Varying the input intensities by a few percent, or varying the H_2 pressure by a few Torr, changes the output phases insignificantly and does not affect the temporal waveform.

The principal approximations of the numerical results, presented in this section, are the assumptions that dephasing is negligible, the driving fields are both quasi-monochromatic and of infinite extent in the transverse direction, and that all molecules are initially in the ground rotational state. The thermal population of states other than $J = 0$ will effectively reduce the molecular coherence. For example, in parahydrogen at room temperature only 44% of the molecules will contribute to the coherence ρ_{ab} and a cell of about twice the length will be needed for broad spectrum generation. For the pulsed excitation we expect our results to apply for a time about equal to the dephasing time, and therefore expect nearly all of the incident power to be converted into the periodic train of subfemtosecond pulses.

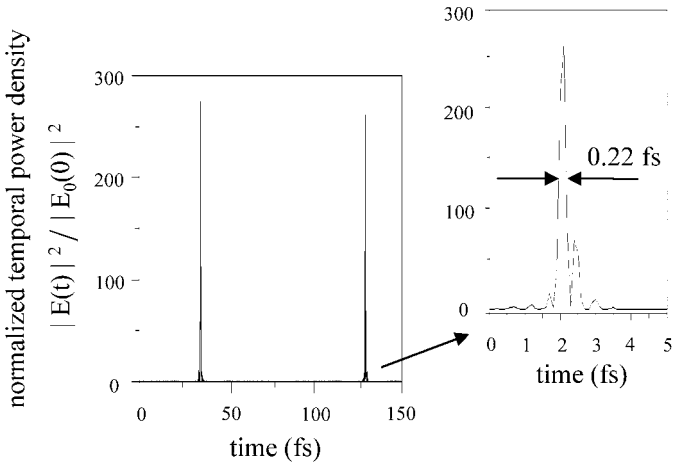

Figure 9. Instantaneous power density of a signal generated in a 14 cm-long H_2 cell at 1 atm and $\rho_{ab} = -0.45$, with sideband phases corrected by an external spectral-phase filter (reprinted from [38] with permission of OSA).

The molecular modulation technique described in this PhD tutorial is quite general and by no means limited to H_2 and D_2 molecules. We have chosen these basic molecules as the first examples, because they have been studied extensively and all of their transition matrix elements are known. Deuterium was selected for our first experiments due to the coincidence of its fundamental vibrational frequency with a frequency difference of convenient laser sources. Possibilities to use more complex molecules are being investigated and look promising, although complications due to thermal population of many molecular states are expected.

5. Subfemtosecond compression of periodic laser pulses

In previous sections we have shown that a coherent molecular oscillation in a relatively thin gaseous medium can cause frequency modulation of laser light and produce a broad spectrum with a possibility of subfemtosecond pulse compression by GVD of the same medium. The proposal relied on driving a Raman oscillation with a beatnote of two quasi-monochromatic laser fields; a characteristic feature of the resulting periodic pulse train was a small pulse spacing (equal to the period of the molecular oscillation, ranging from a few to hundreds of femtoseconds). In this section we describe a source of subfemtosecond pulses with a repetition rate set by a mode-locked laser [39].

The key idea here is to use a mode-locked laser with a cavity length such that a multiple of the longitudinal mode spacing is approximately equal to the Raman frequency (figure 10). When this is the case, the periodic laser pulses drive the coherent molecular motion which, in turn, modulates the refractive index (caused by the electronic transitions) and results in a nearly linear pulse chirp. As the pulses propagate, normal GVD of the same (relatively thin) molecular medium compresses them into the subfemtosecond domain. The requirements on the driving laser are:

(1) the pulse length and the pulse jitter of less than a half-cycle of the molecular oscillation;
(2) adjustable repetition rate, which is much higher than the molecular dephasing rate; and
(3) sufficient intensity.

In this section we first present the formalism and give the FM solution for the ideal case of negligible dispersion. We then proceed with a detailed discussion of experimental parameters and a numerical simulation showing concurrent spectral generation and pulse compression in H_2 (with all the dispersive effects included).

5.1. Analytical solution for the approximate case

We consider one-dimensional propagation of a set of equidistant monochromatic sidebands with the electric field envelopes $E_q(z,t)$, such that the total field is $\hat{E}(z,t) = \sum_q \mathrm{Re}\{E_q(z,t)\exp[\mathrm{j}(\omega_q t - k_q z)]\}$, with $\omega_q = \omega_0 + q\omega_l$, where $\omega_l/(2\pi)$ is a repetition rate of the mode-locked laser ($T = 2\pi/\omega_l$ is a round-trip time of the laser cavity). We assume that the cavity length can be adjusted such that

$$M\omega_l = \omega_m = \omega_b - \omega_a - \Delta\omega,$$

where M is a large integer. The Raman detuning $\Delta\omega$ is the difference of the transition frequency $(\omega_b - \omega_a)$ and modulation frequency ω_m, set by the driving fields. The total space and time quantity for the coherence (off-diagonal density matrix element) of the Raman transition is $\hat{\rho}_{ab}(z,t) = \mathrm{Re}\{\rho_{ab}(z,t)\exp[\mathrm{j}(\omega_m t - k_m z)]\}$; $k_q = \omega_q/c$ and $k_m = \omega_m/c$.

We consider the model molecular system analysed in section 2. We assume that all the molecular population is initially in the ground state and is adiabatically prepared in one eigenstate of the system, such that the coherence ρ_{ab} is given by equation (12). Positive Raman detuning corresponds to all the molecules oscillating in phase with the driving force (the phased state of the molecular system), and negative Raman detuning corresponds to the antiphased state.

We rewrite the slowly varying envelope propagation equation (equation (6) from section 2) for the qth sideband in local time:

$$\frac{\partial E_q}{\partial z} = -\mathrm{j}\eta\hbar\omega_q N(a_q\rho_{aa}E_q + d_q\rho_{bb}E_q + b_q^*\rho_{ab}E_{q-M} + b_{q+M}\rho_{ab}^*E_{q+M}). \quad (26)$$

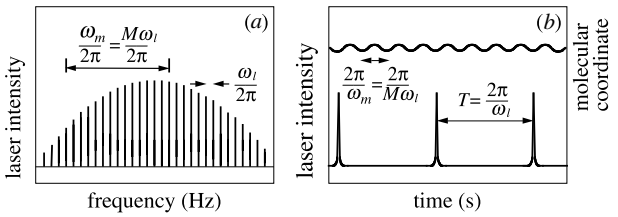

Figure 10. Schematic for the coherent excitation of a molecular oscillation by a periodic pulse train (*a*) in the frequency domain and (*b*) in the time domain. In part (*b*) the upper curve shows oscillations of the molecular coordinate.

The assumptions of negligible dispersion and limited modulation bandwidth allow a self-consistent analytical solution of both density matrix and propagation equations. Similar to section 2, for a boundary condition of a mode-locked spectrum with (real) mode amplitudes $E_q(0)$, each generated sideband amplitude $E_q(z)$ is proportional to a sum of Bessel functions J_n:

$$E_q(z) = \sum_n E_{q-Mn}(0) J_n(\gamma z) \exp\left[-\mathrm{j}\left(\frac{\pi}{2}n + \beta z\right)\right]. \quad (27)$$

The molecular coherence is unaffected by the spectral generation:

$$\rho_{ab}(z) = \rho_{ab}(0) \exp\left(-\mathrm{j}\frac{\omega_m}{\omega_0}\beta z\right), \quad (28)$$

as was emphasized in section 2.3.

In the time domain an equidistant spectrum of Bessel function amplitudes corresponds to an FM signal. Similarly, equation (27) represents a spectrum of a periodic pulse train with a FM carrier. When the applied pulse length and jitter are smaller than the half-cycle of the molecular oscillation, the modulation produces the pulse chirp (figure 11(a)), positive for the phased molecular state and negative for the antiphased state. The pulse compression, therefore, can be accomplished by linear GVD (figure 11(*b*)), possibly in the same molecular medium, as described in section 4. Note that normal GVD would compress negatively chirped pulses (modulated by the antiphased state) and stretch positively chirped pulses.

5.2. Exact numerical solution

We now proceed to the numerical solution of equations (12) and (26), showing concurrent frequency modulation and pulse compression. We consider the fundamental rotational transition in H_2 with $\omega_b - \omega_a = 354\ \mathrm{cm}^{-1}$ (rotation period $T = 94$ fs) and take all molecules in the $J = 0$ ground state. The constants a_q, b_q and d_q include the contributions of all allowed rotation–vibrational transitions in Lyman and Werner bands; the matrix elements are calculated as described in section 4.3.

We envision using a mode-locked Ti:sapphire laser with a pulse length of 20 fs, a repetition rate of 1 GHz and an average power of 1 W, focused into a 20 μm spot size in the H_2 cell. (To facilitate the numerical work, in our simulations we take the repetition rate to be equal to the modulation frequency ω_m, keeping the total bandwidth and average power the same.) We assume that the laser cavity length can be adjusted such that the Raman detuning is $\Delta\omega = -1$ MHz, and stabilized such that the

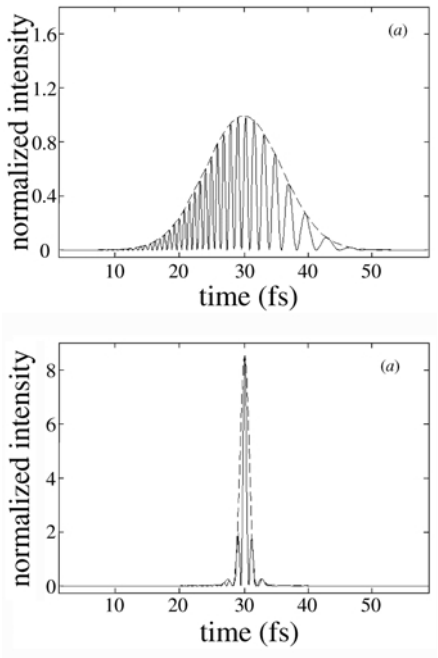

Figure 11. (*a*) Optical oscillations $|E(t)|^2$ (full curve) and the envelope (broken curve) of a femtosecond laser pulse, as modulated by the antiphased molecular oscillation, obtained from the spectrum equation (27) with $\omega_0/\omega_m = 22.5$, $\gamma z = -15$ and a pulse duration of $T/3.8$. (*b*) The same pulse, as compressed by normal linear GVD, in a medium of length given by equation (24). The input field amplitude is normalized to unity (reprinted from [39]).

individual longitudinal mode linewidth is less than 50 Hz. The construction of such a laser is feasible: Demers and DeLucia have developed an 800 MHz self-mode-locked femtosecond Ti:sapphire laser whose mode-lock frequency can be robustly scanned [71]. From their data we deduce the longitudinal mode linewidth of ≈100 Hz. Other authors have demonstrated high repetition rate (⩾1 GHz) [72, 73] and short pulse (⩽10 fs) high power (⩾1 W) mode-locked Ti:sapphire lasers [74, 75] (see also [76–78]).

Figure 12 shows the numerically calculated mode-locked laser pulse compression in H_2 with a density–length product of $2.4 \times 10^{21}\ \mathrm{cm}^{-2}$. At the output of the molecular medium the pulse train maintains its original repetition rate, but each pulse is compressed by a factor of 33, and the peak power is increased by a factor of 10. The calculated FWHM spectral width grows from 730 cm^{-1} at the input to 19 000 cm^{-1} at the output of the medium. In this simulation, the calculated coherence follows closely the ideal analytical solution equation (28), with $\rho_{ab}(0) = -0.05$.

To allow for the coherent adiabatic preparation, we have assumed that the rotational H_2 linewidth is less than $|\Delta\omega| = 1$ MHz. A use of a broader transition would require a larger Raman detuning and a stronger driving laser to prepare high molecular coherence. Very narrow Raman lines may be achieved in novel materials, i.e. solid H_2 [79, 80]. In H_2 gas, the rotational linewidth as narrow as 5 MHz seems to be feasible in the Dicke narrowing regime at low temperature (≈30 K) and pressure (≈0.1 atm) [81–84].

In summary, we predict that periodic femtosecond pulses, obtained from a mode-locked laser, can be significantly

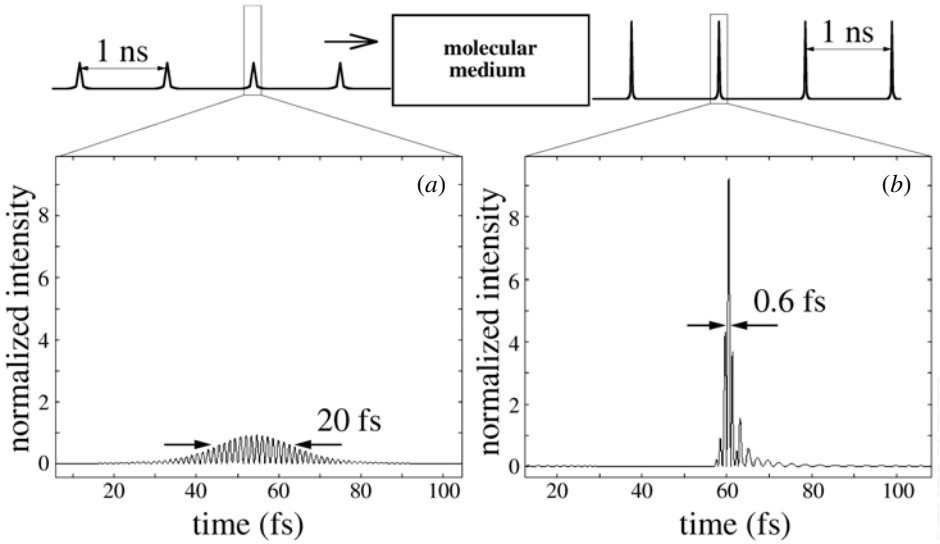

Figure 12. Subfemtosecond compression of periodic laser pulses by rotational modulation in H_2. Laser intensity $|E(t)|^2$ (*a*) at the input of the molecular medium (normalized to unity peak value) and (*b*) at the output of the medium (reprinted from [39] with permission of OSA).

compressed by molecular modulation. While compression into the subfemtosecond domain requires further research into narrow linewidth Raman materials, the proposed method may be able to compete with present techniques for generation of few-femtosecond pulses at high repetition rates. We also note that our technique preserves the narrow mode linewidth of the applied mode-locked laser while extending its total bandwidth, opening new possibilities for high-precision absolute measurements of optical frequencies [85].

6. Experimental demonstration of frequency modulation by phased and antiphased molecular states

In the previous sections we have explained how coherent molecular oscillations can produce laser frequency modulation, with a total bandwidth extending over the infrared, visible and ultraviolet spectral regions, and with a possibility of subfemtosecond pulse compression. The essence of this technique is the use of a Raman transition with a large coherence, established by two collinear single-mode laser fields, tuned slightly below or above Raman resonance so as to excite a single (phased or antiphased) molecular eigenstate. This section describes the first experimental results for this technique. Using molecular deuterium (D_2) we demonstrate collinear generation of a Raman spectrum extending over 50 000 cm^{-1}. The spectrum consists of 17 mutually coherent sidebands, spaced by the fundamental vibrational frequency of D_2 (2994 cm^{-1}), and ranging in wavelength from 2.94 μm to 195 nm [10].

There is prior work on broadband coherent Raman generation. Several groups have studied the enhancement of stimulated Raman scattering by application of the first Stokes component collinearly with the pump laser beam; they have demonstrated increased conversion efficiency, improved reproducibility and small divergence of the anti-Stokes beams [24, 86–88]. Hakuta *et al* [79, 80] have demonstrated collinear Raman sideband generation in solid molecular hydrogen (H_2) and Liang *et al* [89] demonstrated efficient replication of a broadband signal into a different spectral region. Nazarkin *et al* [90] have shown efficient laser frequency modulation by impulsively exciting a coherent vibration of SF_6. In other experiments Ruhman *et al* [91] have used impulsive stimulated Raman scattering to observe coherent molecular vibrations in the time domain. The phased and antiphased excitation technique, and the resultant maximum coherence of a molecular state, have not been discussed.

6.1. Experimental apparatus

In our experiment we use two transform-limited laser pulses at wavelengths of 1.0645 μm and 807.22 nm, such that the (tunable) laser-frequency difference is approximately equal to the fundamental vibrational frequency in D_2. The first laser is a Quanta-Ray GCR-290 Q-switched injection-seeded Nd:YAG laser. Its output (potentially up to 2 J) is attenuated to produce 100 mJ, 12 ns transform-limited pulses at a 10 Hz repetition rate. The laser linewidth is calculated to be $\delta\omega_{laser} = 37$ MHz. The second laser is a lab-built Ti:sapphire system, injection seeded from an external-cavity laser diode and pumped by the second harmonic of a separate Q-switched Nd:YAG laser.

As compared to other such lasers, which were built in the Harris–Yin group earlier [92], our Ti:sapphire oscillator is designed to have a larger mode area, a larger output coupling and a shorter cavity, which allows us to obtain shorter pulses with larger energies. It is interesting to note that, with no focusing elements in the cavity, we are able to obtain a stable large-area TEM00 mode operation (various aspects of laser mode stability are discussed in Siegman's text [93]). This laser produces 75 mJ, 16 ns transform-limited pulses at the seeding laser wavelength. This wavelength can be tuned precisely and is monitored by a Burleigh WA-1500 wavemeter (resolution of 50 MHz). The two driving laser pulses are synchronized by adjusting the delay between the two Nd:YAG laser Q-switch trigger pulses. The laser beams are combined on a dichroic

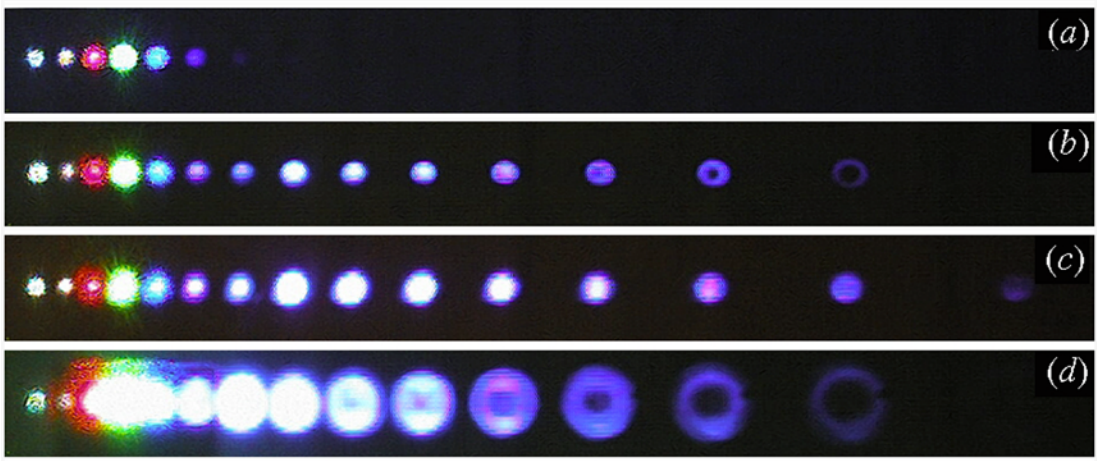

Figure 13. Spectrum produced by the collinear Raman generator at (a) $P = 71$ Torr and $\Delta\omega = -400$ MHz, (b) $P = 71$ Torr and $\Delta\omega = 100$ MHz, (c) $P = 71$ Torr and $\Delta\omega = 700$ MHz and (d) $P = 350$ Torr and $\Delta\omega = 700$ MHz. We observe the two driving infrared fields (on the left), and multiple generated visible and ultraviolet anti-Stokes sidebands. To reduce camera saturation for (*a*)–(*c*), the first four anti-Stokes beams are attenuated by a factor of 100; the driving field at 807 nm and also the fifth anti-Stokes beam are attenuated by 10. For (*d*) the 807 nm beam and the first four anti-Stokes beams are attenuated by 10 (reprinted from [10]).

beamsplitter and are loosely focused to a nearly diffraction-limited spot in a D_2 cell. The 1.06 μm laser spot size is 460 μm and the 807 nm laser spot size is 395 μm.

We determine the Raman resonance by scanning the Ti:sapphire laser frequency and measuring weak Stokes gain at a low pump intensity and a small D_2 density. We observe a consistent 1.5 MHz Torr^{-1} pressure shift of the resonance frequency. The D_2 cell is cooled by liquid nitrogen to $T = 77$ K; the length of the cooled region is 50 cm. Cooling reduces the Doppler linewidth to 260 MHz and increases the population of the ground rotational state of D_2 to 60%. The collisional dephasing linewidth in D_2 at $T = 77$ K is 450 kHz Torr^{-1}, as deduced from room-temperature data [94].

6.2. Observation of the wide spectral comb

When we tune the driving infrared lasers to within 1 GHz from the Raman resonance, we see a bright beam of white light at the output of the D_2 cell. We disperse the spectrum with a prism and project (without collimating or focusing) onto a white scintillating screen (60 cm wide, 270 cm away from the cell). At a D_2 pressure of 50–100 Torr and at a Raman detuning of a few hundred MHz, we observe up to 13 anti-Stokes sidebands and two Stokes sidebands, in addition to the two driving frequencies. These sidebands are spaced by 2994 cm^{-1} and range from 2.94 μm to 195 nm in wavelength. The next Stokes sideband has a wavelength of 24 μm and is difficult to detect. The next (14th) anti-Stokes sideband has a wavelength of 184 nm and is absorbed by air.

Figure 13 shows pictures of the spectrum taken with a digital colour camera with a single-shot exposure at a fixed aperture size. Starting from the left, the first two sidebands are the driving frequencies, and the next four are anti-Stokes sidebands in real colour (red, green, blue and violet); beginning at the fifth anti-Stokes, the sidebands are in the ultraviolet and only fluorescence is visible. Figures 13(*a*)–(*c*) show the spectrum generated at a D_2 pressure of $P = 71$ Torr and a Raman detuning of $\Delta\omega = -400 \pm 25$ MHz in part (*a*), $\Delta\omega = 100 \pm 25$ MHz in part (*b*) and $\Delta\omega = 700 \pm 25$ MHz in part (*c*). The smooth near-Gaussian beam profiles for nearly all sidebands, as shown in figures 13(*a*)–(*c*), demonstrate collinear anti-Stokes generation in a regime of high molecular coherence. At higher pressures the generation is no longer collinear and the anti-Stokes sidebands emerge in circles of increasing diameter. An example at a pressure of 350 Torr and $\Delta\omega = 700$ MHz is shown in figure 13(*d*). We note that the sideband profiles change not only with pressure, but also with the Raman detuning.

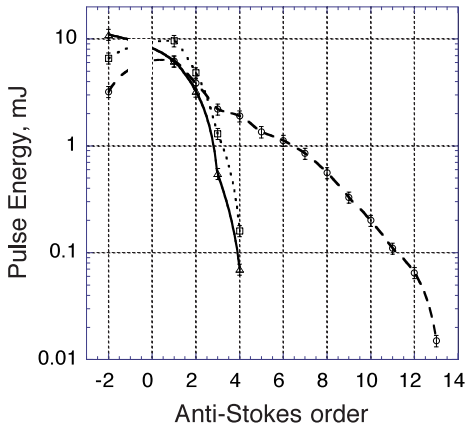

Figure 14. Pulse energies produced by the collinear Raman generator at $P = 72$ Torr. The triangles show on-resonance generation ($\Delta\omega = 0$), the circles show generation by phased ($\Delta\omega = 500$ MHz) and the squares by anti-phased ($\Delta\omega = -200$ MHz) states of D_2 (reprinted from [10]).

Figure 14 shows Stokes and anti-Stokes energy spectra for three different values of the Raman detuning and contrasts the on-resonance generation at $P = 72$ Torr (triangles and full curve) with the generation below resonance (circles and broken curve) and above resonance (squares and dotted curve). We observe that on-resonance generation is less efficient than off-resonance generation for all the anti-Stokes sidebands, and that generation below resonance is more efficient than above resonance. Note that we generate hundreds of μJ/pulses (at a 10 Hz repetition rate) at sidebands far into the UV.

6.3. Collinear off-resonant generation

We now proceed with the discussion of these results. We use the formalism described in section 2. We consider the propagation equation for the Raman sidebands (equation (6)). When the magnitude of the coherence ρ_{ab} approaches its maximum value of 0.5, the coupling terms in equation (6) (last two terms) are of the same order as the dispersion terms (first two terms). In such a high-coherence regime, the generation length becomes comparable to the phase-slip length, and efficient generation proceeds collinearly, with phase matching playing a small role [45]. To the extent that dispersion can be neglected completely, theory predicts a pure sinusoidal frequency modulation of a laser beam, as a result of its propagation through the coherent medium.

The molecular eigenstate which evolves from the ground state as the field amplitudes are increased, and the coherence ρ_{ab} which is obtained from it, are given by equations (10) and (12), respectively. When the Raman detuning is larger than the driving laser linewidth, the molecular system follows this eigenstate adiabatically, with the sign of ρ_{ab} determined by the sign of the Raman detuning. In a resonant, nonadiabatic regime the molecules exhibit two-photon Rabi flopping at a frequency B.

In our experiment the Doppler broadened linewidth (260 MHz) of the 2994 cm^{-1} transition of D_2 is larger than both the collisional dephasing rate (32 MHz for $P = 72$ Torr) and the laser linewidth (37 MHz). When we tune close to the centre of the Doppler line, we expect adiabatic preparation for most of the molecules in both wings of the velocity distribution, with significant magnitude of their excitation when the coupling parameter $B > \delta\omega_{laser}$. The phases of these excitations are positive or negative depending on the sign of the Raman detuning, such that the contributions of these molecules partially cancel each other, resulting in a smaller integrated value of the coherence ρ_{ab} at the centre frequency. Conversely, when we detune to either side of the Doppler line, we expect adiabatic preparation of nearly all of the molecules in the same (phased or antiphased) state, resulting in a larger total coherence and more efficient Raman generation. Similar behaviour has been observed in saturated coherent anti-Stokes Raman spectroscopy [95].

6.4. Raman generation by adiabatic states

Figure 15 illustrates the behaviour described in the previous paragraph. Parts (*a*) and (*b*) show the first anti-Stokes pulse energy as a function of the Raman detuning, both at low pressure ($P = 6$ Torr). Here, the depletion of the applied fields is not important, and the generated energy is proportional to the square of the Doppler-averaged coherence (equation (6)). In figure 15(*a*) the 1.06 μm laser pulse energy is 5.4 mJ and $B = 39$ MHz $\approx \delta\omega_{laser}$; for these conditions the anti-Stokes generation peaks on resonance. For figure 15(*b*) we apply full power of the driving lasers, so that $B = 168$ MHz $\gg \delta\omega_{laser}$, and observe that the anti-Stokes generation peaks on both sides of the resonance, with a dip exactly on resonance. The peak at positive $\Delta\omega$ is higher, because as the laser power increases as a function of time, this peak Stark-shifts toward resonance. We solve the full density-matrix equations numerically for the experimental driving laser pulses, calculate the (complex) coherence ρ_{ab} at the pulse peak for different values of Raman detuning, and average it over the Doppler distribution. The full curves in figures 15(*a*) and (*b*) show the square of the Doppler-averaged coherence (no scaling). We calculate that the maximal value of the coherence that we achieve in our experiment is $|\langle\rho_{ab}\rangle_{Doppler}| = 0.33$.

Figure 15(*c*) shows qualitatively similar behaviour at a higher D_2 pressure ($P = 72$ Torr). The filled circles represent the sum of all generated Stokes and anti-Stokes sidebands. The open circles and triangles show the first and second anti-Stokes sidebands. All measurements for figures 14 and 15 are done with a Molectron J4-09 pyroelectric detector. Each point in the plots is an average over 8 laser shots, with error bars showing the standard deviation for each data set.

In order to investigate adiabatic and nonadiabatic molecular excitation we measure the total laser energy transmitted through the D_2 cell (including all applied and generated sidebands) as a function of the Raman detuning. When the molecular evolution is adiabatic, we expect all molecules to return to the ground state as the laser fields decrease at the falling edge of the applied pulses. We observe a dip in transmission on Raman resonance, confirming that energy is left in the molecular system due to nonadiabatic behaviour. For comparison we numerically calculate the probability for the molecular system to remain in the adiabatic eigenstate $|+\rangle$ (equation (10)), averaged over the Doppler distribution (full curve in figure 15(*d*)), again demonstrating a good qualitative agreement between theory and experiment. Comparing figures 15(*c*) and (*d*) we note that the Raman generation peaks at detunings where the molecular evolution is completely adiabatic.

In order to ascertain that the laser energy is indeed deposited into the molecular system, we literally listen to the molecular excitations. We put a commercial dynamic audio microphone into the D_2 cell and measure the amplitude of the shock wave produced by the laser energy, which is absorbed through the Raman excitation. Figure 15(*e*) shows the acoustic signal as a function of the Raman detuning; we observe a dependence complementary to that of figure 15(*d*). We attempt an absolute calibration of the microphone by measuring a sound wave produced by an 8 mJ, 1.06 μm laser pulse hitting black laser-burn paper inside the D_2 cell. We find, perhaps fortuitously, that the measured energy, required to produce the shock wave (7 mJ), is within a factor of two of the total laser energy, absorbed through the resonant Raman process (12 mJ).

7. Single-sideband conversion by a rotating molecular waveplate

Four-wave mixing in atomic and molecular gases has served, for over 30 years, as an efficient tool, producing coherent radiation at desired wavelengths [97, 98]. An important development in this area was the invention of nonlinear optics (NLO) at maximal coherence [45, 99], which allowed 100% frequency conversion without the need for phase-matching, under conditions where the nonlinear susceptibility is of the order of the linear susceptibility. This technique relied on all-resonant laser pulse propagation in an atomic medium (Λ scheme) and utilized EIT [43].

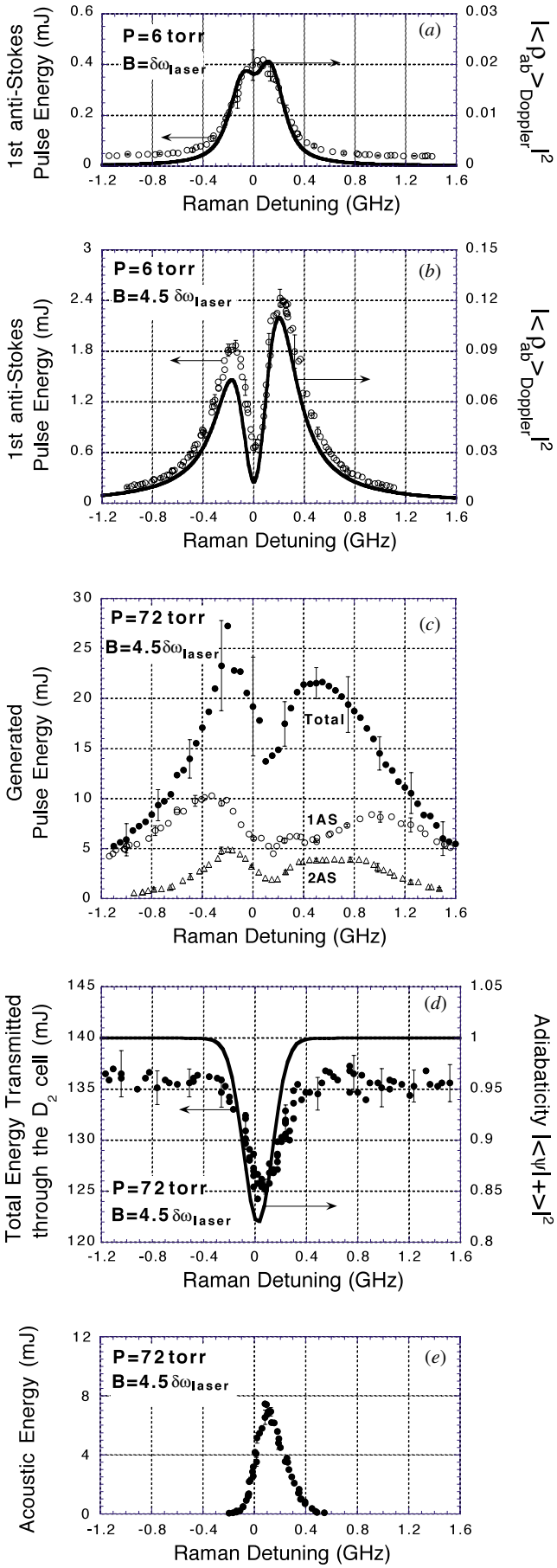

Figure 15. Raman generation by adiabatic eigenstates in D_2. (*a*) First anti-Stokes generation by weakly driven vibrations ($B \approx \delta\omega_{laser}$) at $P = 6$ Torr. (*b*) First anti-Stokes generation by strongly driven vibrations ($B \gg \delta\omega_{laser}$) at $P = 6$ Torr. In both (*a*) and (*b*) the full curves show the calculated square of the Doppler-averaged coherence ρ_{ab} at the pulse peak. (*c*) Sum over pulse energies of all generated Raman sidebands (filled circles), first anti-Stokes generation (open circles) and second anti-Stokes generation (triangles) for $B \gg \delta\omega_{laser}$ and $P = 72$ Torr. (*d*) Total energy in all applied and generated sidebands at the output of the D_2 cell. The full curve represents the calculated fraction of the molecular population in the eigenstate which evolves adiabatically from the ground state. (*e*) Acoustic signal, which is proportional to the resonant nonadiabatic molecular excitation, as a function of Raman detuning.

In this tutorial we have shown that the ideas of EIT and NLO at maximal coherence can be extended to molecular systems. In such systems the laser detunings from electronic states are very large, but a Raman transition can still be adiabatically prepared in a maximal-coherence state, by using two single-mode laser fields at a finite Raman detuning. When this coherence is established, the molecular motion modulates light in the same way as a conventional optical modulator, but at a frequency many orders of magnitude higher. In our experiments, described in section 6, strongly driven molecular vibrations were used to produce frequency modulation with an ultrabroad bandwidth. For many applications, however, single-sideband conversion is preferred. In this section, we show how the molecular modulation technique can be modified to achieve efficient frequency conversion into a single sideband [46].

The idea is simple, when explained by analogy to conventional optical modulators. It is known that a rotating birefringent waveplate will modulate circularly polarized light to produce a single sideband, shifted by twice the rotational frequency of the waveplate. For a diatomic molecule (D_2 in our case) the polarizability depends on the orientation of the molecular axis; thus we can create a rotating waveplate by aligning all the molecules in the D_2 cell and making them rotate in unison.

7.1. Molecular excitation by circular polarizations

The rotating molecular waveplate is created by a coherent excitation of an ensemble of molecules, which are initially in the ground molecular state ($v'' = 0$, $J'' = 0$), into a superposition of a molecular vibration and rotation ($v' = 1$, $J' = 2$). Ideally, we want to establish an oscillation with the maximum coherence at this transition frequency, with a 50/50% probability for a molecule to be in the ground state or in the excited ro-vibrational state. We use two strong laser fields with opposite circular polarizations, slightly detuned from the Raman resonance in order to excite this coherent molecular oscillation. This oscillation, in turn, mixes with a third circularly polarized (potentially widely tunable) laser field and generates a single Raman sideband. In this case, the single-sideband conversion is required by the angular momentum conservation. Unlike our previous molecular modulation experiments, no further generation will occur when only the two strong circularly polarized drive fields are applied.

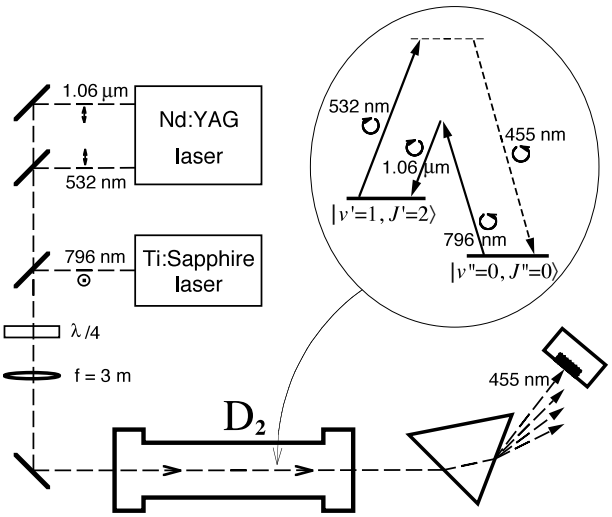

Figure 16. Experimental set-up and energy level diagram for frequency conversion in D_2. We use two laser fields (1.06 μm and 796 nm), with opposite circular polarizations, to produce a ro-vibrational excitation, which converts a third field (532 nm) into a single sideband (455 nm).

(In a related work, Holmes and Flusberg [100] have derived the dependence of Raman gain on light polarization, phase mismatch and frequency offset; and Villeneuve *et al* [101] have demonstrated efficient excitation of high-J molecular states by an optical centrifuge.)

Our experimental set-up is shown in figure 16. We use the same two lasers as in the experiments described in section 6. These lasers produce transform-limited laser pulses at wavelengths of 1.0645 μm and 796.12 nm, such that the laser frequency difference is approximately equal to the frequency of the $(v' = 1, J' = 2) \rightarrow (v'' = 0, J'' = 0)$ molecular transition in D_2. The first laser (Quanta-Ray GCR-290 Nd:YAG) produces 150 mJ, 10 ns pulses, and the second laser (our custom-made Ti:sapphire system, pumped by the second harmonic of a separate Q-switched Nd:YAG laser) produces 75 mJ, 14 ns pulses at the (tunable) seeding laser wavelength. The two driving laser pulses are synchronized by adjusting the delay between the two Nd:YAG laser Q-switch trigger pulses. The third (weak) laser pulse (0.8 mJ, 7 ns) at 532 nm is obtained from the second harmonic of the first Nd:YAG laser and is thus automatically synchronized with the two driving pulses. Initially all three beams are linearly polarized, with the polarization of 1.06 μm and 532 nm beams in the horizontal plane and the polarization of the 796 nm beam in the vertical plane. The laser beams are combined with dichroic beamsplitters and sent through a $\lambda/4$ Fresnel rhomb which produces opposite circular polarizations for orthogonal linear polarizations at the input. The beams are focused into the D_2 cell; the 1.06 μm laser spot size is 460 μm, the 796 nm laser spot size is 395 μm and the 532 nm laser spot size is 195 μm. The D_2 cell is cooled by liquid nitrogen to $T = 77$ K, such that 60% of the molecules are in the ground rotational state. The length of the cooled region is 48 cm and the pressure is 103 Torr.

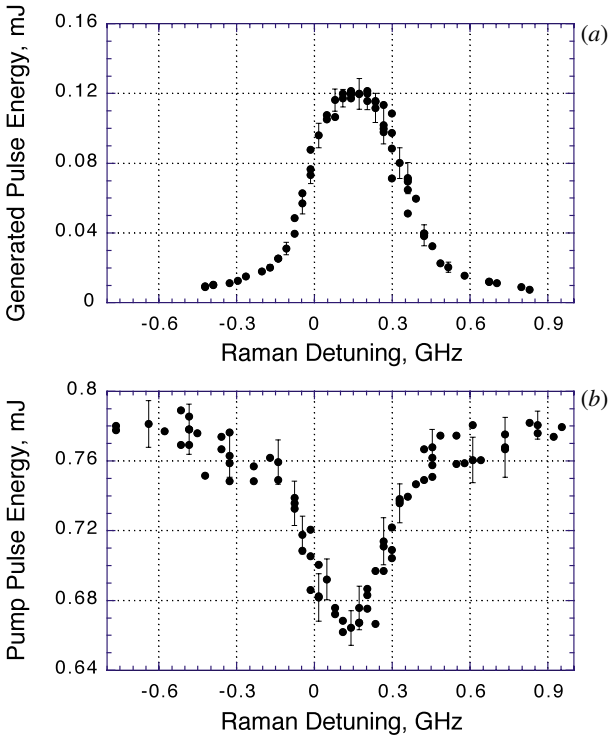

Figure 17. Tuning characteristics of the molecular frequency converter: (*a*) pulse energy, generated at 455 nm; (*b*) pulse energy in the 532 nm pump field. The energy conversion efficiency is 15.4% and, within error bars, the pump depletion is equal to the generated energy (reprinted from [46] with permission of OSA).

7.2. Efficient single-sideband conversion

We observe collinear generation of a single sideband at 455 nm, at a circular polarization which is orthogonal to the polarization of the 532 nm beam. We disperse the sidebands with a prism and use a Molectron J4-09 pyroelectric detector to measure the generated pulse energy. Figure 17(*a*) shows the pulse energy at 455 nm as a function of the Raman detuning of the driving fields. Zero detuning is determined from the position of the generation peak at reduced driving intensities. For comparison, figure 17(*b*) shows the depletion of the 532 nm beam. Each point in the plots is an average over 10 laser shots, with error bars showing the standard deviation for each data set. With the correction for the quantum defect (1.17:1) the energy absorbed from the 532 nm beam equals (within error bars) the generated energy at 455 nm. This demonstrates single-sideband frequency conversion, with the peak energy conversion efficiency of 15.4% (and the photon conversion efficiency of 13.2%).

7.3. Relation to previous work

In the past, researchers have done significant work in the areas of Raman processes and four-wave mixing in both atoms and molecules [97, 98]. Oudar and Shen [102] have discussed in detail how four-wave mixing can be used for spectroscopy. Byer and his coworkers [103] have developed coherent anti-Stokes Raman scattering into an effective spectroscopic tool. Ducuing *et al* and Loy *et al* [104, 105] have demonstrated four-wave mixing using vibrational transitions in molecules to obtain tunable infrared radiation.

Our technique significantly differs from this past work. Our conversion process occurs collinearly, at low pressure, off line centre, without the need for phase-matching, and results in good spatial and temporal coherence of the generated field. As opposed to traditional Raman scattering, our generation process is linear in the pump (532 nm) field intensity and allows efficient conversion of radiation from a weak pump.

Our technique requires preparation of high molecular coherence. In that sense our work is related to the research on ultrafast coherent excitation of superposition states in molecules, performed by Laubereau *et al* [106]. These authors demonstrated four-wave mixing by a superposition of molecular vibrations and employed it to measure the coherence time of the vibrational state. In contrast to our work, their coherence was achieved non-adiabatically, through the application of an intense broadband short pulse.

As mentioned earlier, there is a strong similarity between our technique and that of nonlinear optics at maximum coherence in atomic lead (Pb), which utilizes EIT [45, 99]. Though the preparation and nature of the coherence in the molecular system differs from that in Pb, the generation equations are nearly the same and predict the possibility of 100% photon conversion from the third applied field to the generated field.

The results of this experiment are below the ideal limit by a factor of 7.6. We believe this discrepancy is due to a lower than expected coherence of the ro-vibrational transition, most likely caused by the dephasing of the ro-vibrational state ($v' = 1$, $J' = 2$). By using shorter pulses or operating at lower pressures with a longer interaction length (perhaps with a multi-pass cell), we expect to approach the theoretical maximum.

In contrast to the EIT work, our technique does not require a single-photon resonance for the two driving fields, and the third applied field is far detuned from the upper electronic states. The large detuning should result in a conversion efficiency which is relatively insensitive to the bandwidth or wavelength of the applied third source. This leads to a potential application for the generation of tunable far-infrared radiation (related work on infrared conversion is given in [107, 108]).

7.4. Application to far-IR generation and detection

Far-infrared generation and detection is of large interest in modern chemistry, biology and astronomy; thus we consider infrared conversion as the most important potential application of the technique described in this section. In our configuration (figure 16), instead of using 532 nm radiation, one can apply tunable near-infrared radiation (3–4 μm) of correct polarization to downshift to tunable far-infrared radiation (30–300 μm). Under the assumption of large single-photon detunings, at a fixed density and length, the energy conversion efficiency will decrease as the square of the frequency of the generated field, but still has the possibility of being larger than that of any other technique. Moreover, the same method may be used to convert laser pulses from far-infrared into near-infrared, thereby making their detection much more efficient. This idea was anticipated by the time-resolved infrared spectral photography of Bethune *et al* [109]. We imagine building an infrared spectrometer which utilizes molecular modulation to generate far-infrared, sends the far-infrared radiation through the test medium, and then converts it back into the more easily detectable radiation using the same molecular system.

8. Generation and detection of AM and FM light at 90 THz modulation frequency

It is well known that a carrier and two sidebands, depending on their relative phases, correspond to a FM or AM signal. Light is most often modulated by driving the dielectric constant of a material so as to produce phased sidebands with a frequency spacing of, at most, 150 GHz. In this section we describe spectral synthesis of AM and FM light with a sideband spacing, and therefore modulation frequency, equal to the fundamental vibrational frequency of molecular deuterium (2994 $\mathrm{cm}^{-1} \approx 90$ THz). This is a first step toward the synthesis of subfemtosecond pulses with prescribed temporal shape [40].

As a light source for this experiment we use our collinear Raman generator, described in section 6. We separate out and use only three sidebands (1.06 μm, 807 nm and 650 nm) from the Raman comb. FM or AM light is obtained by manually adjusting the relative phases of these sidebands. To detect this modulation we make use of the fact that a Raman transition is driven by the near-resonance component of the temporal envelope of the applied light intensity. These sidebands may be phased so that this component is either zero (FM) or maximized (AM). Note that it is essential that three sidebands be used in an experiment of this type. If two sidebands are used, as in coherent anti-Stokes Raman spectroscopy [97], then the magnitude of the envelope is independent of phase.

8.1. Spectral synthesis and detection of AM and FM light

We extend our experimental set-up as shown in figure 18. We use a prism to disperse the sidebands, obtained from the collinear Raman generator, and retain those with wavelengths 1.06 μm, 807 nm and 650 nm. A partial reflector is used to attenuate the 1.06 μm beam, so that following the attenuation the ratio of the intensities of these beams are 1:14:1.2, respectively. The phase of the 650 nm beam is varied by tilting a glass plate (thickness 1.0 mm). The beams are then retroreflected and recombined into a new region of the D_2 cell.

This new region of the D_2 cell works as a detector for the AM component of the waveform. As the force on the nuclei is proportional to the electric field squared, and as the nuclei are too heavy to respond to the fast optical oscillations, the molecules respond to the variations in the intensity of light. The molecular motion, in turn, mixes with the 650 nm beam to generate the next anti-Stokes sideband at 544 nm. We measure the dependence of the intensity at 544 nm on the phase of the 650 nm beam.

In the 'detector' region of the cell, the ensemble-averaged molecular oscillation is described by a normalized coordinate $\langle X \rangle = \rho_{ab} \cos(\omega_m t)$, where $\omega_m = 2994\ \mathrm{cm}^{-1}$. The magnitude $|\rho_{ab}|$ is proportional to the sum of the cross-products of the adjacent field amplitudes (equations (2), (9) and (12))

$$|\rho_{ab}|^2 \propto |E_0 E_{-1}^* + E_1 E_0^*|^2 \propto 1 + \frac{2|E_{-1}||E_1|}{|E_{-1}|^2 + |E_1|^2} \cos(\varphi), \quad (29)$$

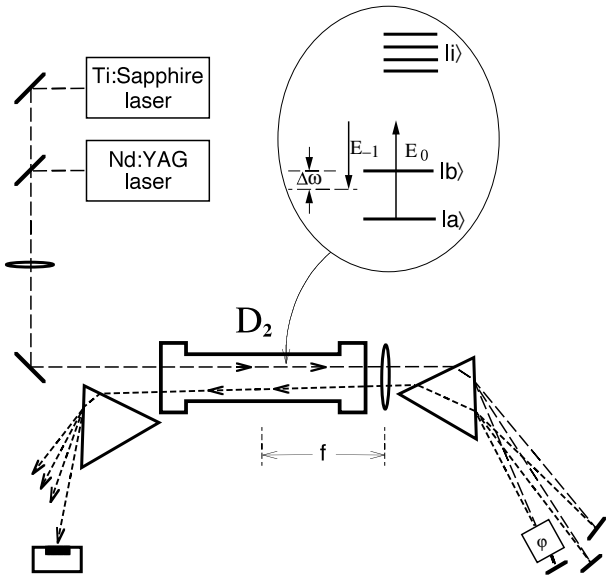

Figure 18. Experimental set-up and energy level diagram for collinear Raman generation, synthesis of FM and AM light and detection of the modulation.

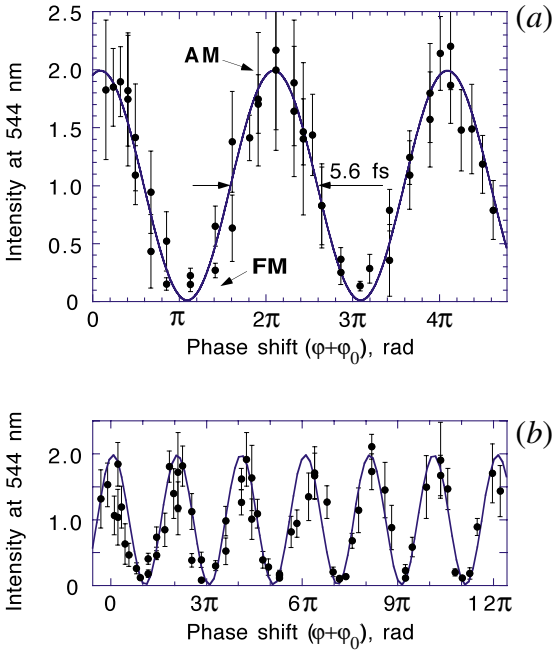

Figure 19. Anti-Stokes generation at 544 nm (arbitrary units) as a function of the relative phase φ of the three sidebands (at 1.06 μm, 807 and 650 nm). (*a*) Data set 1. (*b*) Data set 2, showing that additional phase retardation does not reduce the contrast. The full curve is produced from equation (29) by adjusting the vertical scaling and the experimentally unknown initial relative phase of the sidebands φ_0 (reprinted from [40]).

where, following the notation of section 2, E_{-1}, E_0 and E_1 are the (complex) field amplitudes of 1.06 μm, 807 nm and 650 nm fields, respectively. The relative phase of the three sidebands is defined as $\varphi = \arg(E_1 E_0^*) - \arg(E_0 E_{-1}^*)$.

8.2. Discussion of the experimental results

The two terms in equation (29), which drive the molecular oscillation, will interfere either constructively or destructively, depending on the relative phase of the sidebands. Figure 19 shows the interference fringes (at 26 Torr D_2 pressure, Raman detuning $\Delta\omega = 800$ MHz), produced by measuring the peak intensity of the generated anti-Stokes field (at 544 nm) as a function of the relative phase φ of the three driving fields. (As follows from equation (6), in the small-signal limit this intensity is proportional to the molecular coherence $|\rho_{ab}|^2$.) Each data point is an average over 10 laser shots, with error bars showing the standard deviation for each set. The experimental data is fitted by a theoretical curve produced with the assumption of perfect mutual coherence among the three sidebands and a constant ratio $|E_1/E_{-1}|$ (equation (29)). The adjustable parameters in this fit are the vertical scaling and the initial phase φ_0. The ratio $|E_1/E_{-1}| = 1.1$ is measured experimentally and the phase shift is calculated precisely from the parameters of the glass plate. The good quality of the fit represents the proof of the near-perfect mutual coherence among the three sidebands across both their spatial and temporal profiles.

Although it was expected that sidebands, obtained from the collinear Raman generator, are mutually coherent, until now it was not clear if their relative phases remain the same across temporal and spatial profiles. It is this uniform mutual coherence among the sidebands that allows the synthesis of AM and FM light, and in the future will lead to the generation of subfemtosecond pulses.

In the time domain, three sidebands spaced by 2994 cm^{-1} synthesize a periodic waveform with an 11.1 fs period (equal to the molecular oscillation period). When $\varphi = \pi$ (and $|E_1/E_{-1}| = 1$) the field intensity is constant, the waveform is purely FM and does not excite the molecular oscillation (this situation corresponds to the minima of figure 19). When $\varphi = 0$ the waveform is purely AM and efficiently drives the molecules at their resonant frequency (this situation corresponds to the maxima of figure 19).

From a different point of view, the plot of figure 19 can be considered as a time correlation of two beatnotes: $(E_{-1} + E_0)$ and $(E_0 + E_1)$. A 2π shift in the relative phase φ corresponds to an 11.1 fs time delay between the beatnotes. We use this relation to calculate the time delay from the relative phase in figure 19. The full width at half-maximum (FWHM) of a single peak in figure 19 corresponds to exactly half of the molecular period, 5.6 fs. It should be noted that, if we use filters to make the intensities of the three sidebands equal and adjust $\varphi = 0$, we will produce periodic pulses with a FWHM duration of (11.1 fs)/3 = 3.7 fs.

8.3. Molecular phase spectroscopy

We now use the techniques of this section to further characterize the collinear Raman generator. In particular, we show that the phase of the molecular coherence, and therefore of the generated sidebands, changes by π when the difference of the two input frequencies is tuned from below to above the molecular resonance. This measurement is made as follows: working at a D_2 pressure of 20 Torr, we step through a sequence of Raman detunings and, at each detuning, tilt the glass plate so as to obtain a minimum in the fringe pattern. At each point

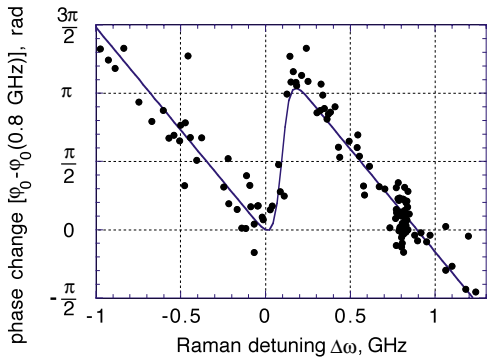

Figure 20. Molecular phase spectroscopy: relative shift of the fringe pattern of figure 19 versus Raman detuning. The full curve shows a linear dispersion slope and a π-radian phase step-up on resonance.

the tilt angle is converted into phase retardation at 650 nm. We find that mechanical shifts of the retro-reflecting mirrors cause a slow drift of about 1 rad/10 min. We therefore intermittently measure the tilt angle which is necessary to cause a minimum at a Raman detuning of 800 MHz and subtract this drift from our data.

Figure 20 shows the relative shift of the fringe pattern as a function of the Raman detuning. We observe a linear dispersion slope, caused by the difference in the beam path length for the three sidebands (in our set-up the path for 807 nm beam is 9.8 cm longer and this delay is calculated to produce the dispersion of -4.1 rad GHz^{-1} in figure 3(*a*)). In addition, we observe a distinct π-radian change in this shift, when tuning from one side of the Raman resonance to the other. This phase change corresponds to the transition from phased (driven below natural resonance) to antiphased (driven above natural resonance) molecular eigenstate [40].

The π-radian step-up in figure 20 constitutes a direct observation of the phase reversal at the transition between phased and antiphased states. Moreover, at low D_2 pressure (in the limit of small depletion of the driving fields and negligible dispersion) the amplitude of the generated anti-Stokes field is proportional to the (complex) coherence $E_1 \propto -\mathrm{j}\rho_{ab}E_0$ (see equation (6)). Thus by measuring the relative phase of the generated and driving fields we can measure the phase of the coherence ρ_{ab}. Therefore, one can use the set-up of figure 18 to measure the phase of the coherence as a function of the Raman detuning, in a method complementary to the traditional spectroscopic techniques.

8.4. Molecular Fourier analyser for ultrashort pulses

The idea of detecting the resonant AM component of a waveform by its ability to excite a Raman transition can be extended to systems with a large number of transitions. Based on this idea, we propose a technique for determining the ultrashort pulse shapes. The essence of the technique is the following: when an electromagnetic wave is applied to a Raman medium, a particular Raman oscillation is driven by the corresponding Fourier component of the wave envelope. Thus the information about the pulse shape and duration can be extracted by measuring relative excitations of a set of Raman transitions.

We envision a multi-component system with a set of Raman transitions at a variety of frequencies. The pulse, which is to be measured, is applied to the Raman system, without the need for potentially dispersive beamsplitters required for autocorrelation. Then a long probe pulse is used to read-out the Raman coherence. The resultant Raman spectrum is analysed, yielding the magnitudes for the Fourier components of the intensity envelope of the tested short pulse.

We note that, although one would need an infinite number of Raman transitions to fully characterize the pulse envelope, useful information could be extracted with a limited set of transitions, given that the Raman oscillations are fast enough to respond to the ultrashort pulse. For example, the pulse duration can be bounded by using just a few transitions.

9. Multiphoton ionization with single-cycle pulses

We proceed to the description of our multiphoton ionization experiment, which became a high point of this PhD work. As noted in the introduction, the development of our new light source was largely motivated by the possibility to extend ultrafast measurements to the timescale of electronic motion. Multiphoton ionization on a few-femtosecond timescale, under conditions where photoionization requires 11 photons of the lowest frequency and 5 photons of the highest frequency of the spectrum, is a first step toward this goal [11].

9.1. Experimental set-up and ion detector calibration

Figure 21 shows our experimental set-up. The apparatus for broadband collinear Raman generation was described in detail in sections 6 and 8. In this experiment we use two synchronized transform-limited laser pulses (typically 80 mJ/15ns at a 10 Hz repetition rate) at wavelengths of 1.06 μm (fixed) and 807 nm (tunable). The laser frequency difference is tuned 0.6 GHz below the fundamental vibrational frequency in D_2 (2994 cm^{-1}). The laser beams are combined on a dichroic beamsplitter and loosely focused into a D_2 cell (with a D_2 pressure of 38 Torr). We disperse the cell output spectrum with a prism and select five sidebands, ranging from 1.06 μm in the infrared to 468 nm in the blue. Each sideband is retro-reflected through the prism, such that the spectrum is recombined in a slightly offset beam, which is picked off by a small mirror. Sideband energies in the combined beam are: 33 mJ (at 1.06 μm), 28 mJ (at 807 nm), 4.2 mJ (at 650 nm), 0.9 mJ (at 544 nm) and 0.2 mJ (at 468 nm). We adjust sideband phases by tilted glass plates and focus the recombined beam into low-pressure (3×10^{-5} Torr) Xe gas.

The number of ions is measured with a channeltron detector. The ion signal, in all following figures, is given in relative units. One relative unit corresponds to (roughly) 42 ions per laser shot, produced at 3×10^{-5} Torr Xe pressure. Each data point is averaged over about a hundred laser shots. For the conditions of our photoionization experiment, we estimate the focal volume to be roughly 10^{-4} mm^3, such that at 3×10^{-5} Torr pressure the number of Xe atoms in the focal region is $\approx 10^5$. In our experiments, in order to increase the dynamic range of ion detection, we vary Xe pressure and normalize the signal to Xe concentration. According to our calculations, the ionization rate, which corresponds to one relative unit in our plots, is of the order of 3×10^{-4} /(10 ns).

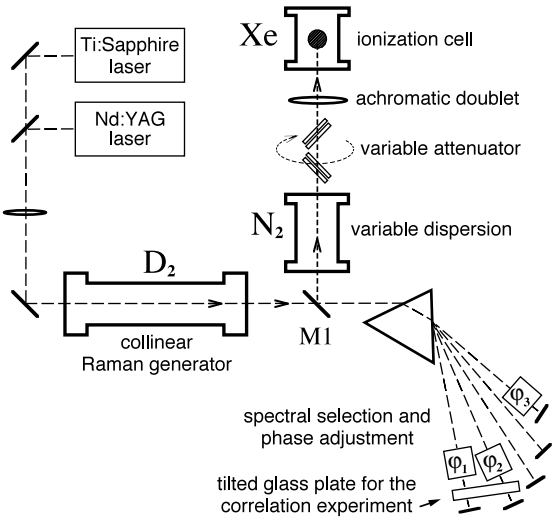

Figure 21. Experimental set-up for multiphoton ionization of Xe with five Raman sidebands (at 1.06 μm, 807, 650, 544 and 468 nm). The mirror M1, which is displaced in the vertical plane, picks off the slightly offset retroreflected beam. We vary sideband phases independently with tilted glass plates, or by varying dispersion in the N_2 pressure cell.

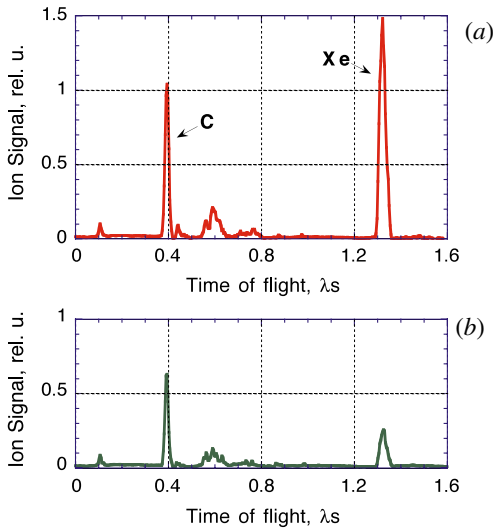

Figure 22. Time-of-flight mass spectroscopy of the photoionized species, detected in the Xe cell in the set-up of figure 1. In addition to a distinct Xe peak we observe peaks that correspond to lighter species. Spectrum (*a*) is recorded with sideband phases adjusted to maximize Xe ionization; spectrum (*b*) is recorded with sideband phases adjusted to minimize Xe ionization (reprinted from [11]).

9.2. Selective ion production

In our experiment, different chemical species are selected according to their masses, by measuring their time of flight from the laser focal point to the channeltron detector. Figure 22 shows the mass spectrum of ions produced by the multicolour beam. In addition to a distinct Xe peak we observe several other peaks which correspond to species with smaller atomic masses. We determine that the largest of these impurity peaks corresponds to carbon (C) (atomic weight of 12).

As a first example of spectral phase sensitivity, we demonstrate selective ion production. By varying only the phases of the applied sidebands, we achieve a large change in the relative magnitude of C and Xe ionization rates (parts (*a*) and (*b*) of figure 22). At a fixed total laser pulse energy, the ratio of the number of Xe ions to the number of C ions changes from 1.4 (figure 22(*a*)) to 0.4 (figure 22(*b*)). We believe that the change in the Xe:C ratio is a result of the stronger dependence of Xe ionization rate on the peak electric field amplitude of the temporal waveform.

9.3. Number of photons required for ionization: 5 or 11?

Next, we zoom in on the Xe peak and use a boxcar integrator to measure the total Xe ion signal produced by each laser shot. We observe large contrast in Xe photoionization (up to a factor of 15), as we change the sideband phases. We expect the ion signal to maximize when the sidebands are phase-locked and synthesize a train of pulses with high peak intensity. When spectral phases are changed, the peak intensity reduces and the probability of multiphoton ionization decreases. Note that this argument is not straightforward, because even the order of the process is not clearly defined: it would take eleven photons of the lowest frequency and five photons of the highest frequency of the applied spectrum to ionize Xe atoms.

In order to determine the power law for the ionization process, we measure the ion yield as a function of the total applied laser energy (with relative spectral energies fixed as noted above). We use a wavelength-independent variable attenuator. The attenuator is composed of four fused-silica plain-parallel plates, inserted into the combined multicolour beam (figure 21) and tilted by approximately 45° with respect to the beam. The plates are rotated around the axes of the beam to provide variable transmission for linearly polarized sidebands. At these conditions, the attenuation of different spectral components is approximately equal.

Figure 23 shows the dependence of the Xe ion signal on total pulse energy (summed over five sidebands). Three sets of data in the figure correspond to different relative phases among the sidebands, or equivalently, to different temporal shapes of the waveform. For set 1 (circles) we adjust sideband phases to maximize the Xe signal (phase-locked spectrum). For set 2 (squares) we change the phase of the 1.06 μm beam by π. For set 3 (triangles) we return the phase of the 1.06 μm beam to its original value and change the phase of the 468 nm beam by π. For all three cases the data fits well to a sixth-order power law (full (set 1), broken (set 2) and dotted (set 3) lines in figure 23). We estimate our experimental uncertainty here to be plus/minus one order. We conclude that, at our experimental conditions, the sixth-order channel dominates in the photoionization process, with possible contributions from the fifth and seventh-order channels. The important observation is that, to the precision of our measurement, the order of the ionization process does not depend on the laser pulse shape. The ion yield, at a fixed laser energy, changes as a function of the temporal shape. But at a fixed pulse shape the slope of the ion signal versus laser energy (on a log–log scale) does not depend on the temporal structure.

9.4. Ionization used to characterize single-cycle pulses

9.4.1. Cross-correlation measurements. We can now use the pulse-shape sensitivity of the photoionization to characterize

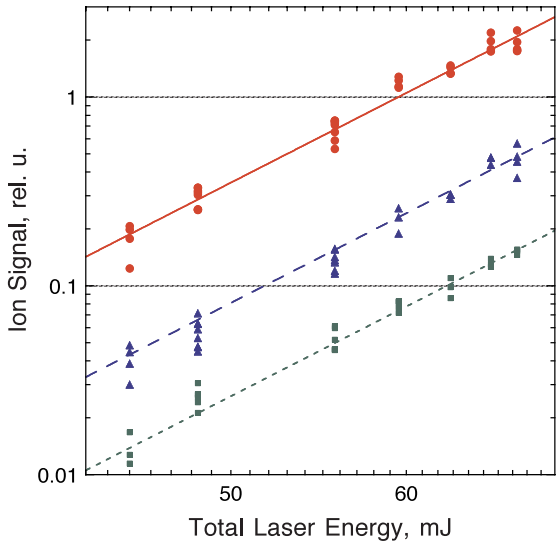

Figure 23. Multiphoton ionization of Xe with spectral bandwidth such that the ionization requires eleven photons of the lowest frequency and five photons of the highest frequency. The ion yield is shown as a function of total energy in laser pulses. Three sets of data, which correspond to different temporal pulse shapes, are all fitted by a sixth-order power law (reprinted from [11]).

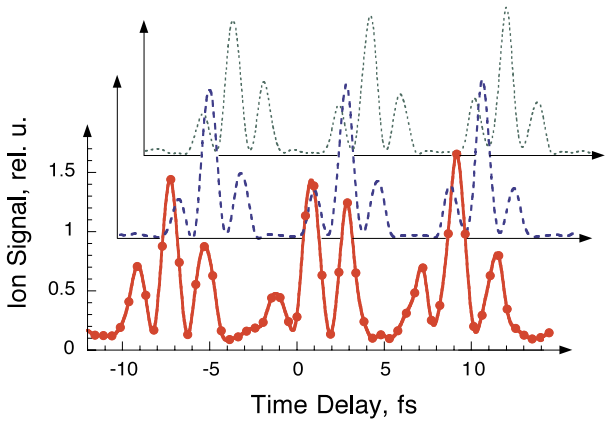

Figure 24. Correlation of waveforms, synthesized by subsets of Raman sidebands: experiment (full curve) and theory (broken and dotted curves) (reprinted from [11]).

our light source. We perform cross-correlation measurements in a collinear configuration. We vary the delay of the 468 and 544 nm beams with respect to the 650 nm, 807 nm and 1.06 μm beams. We do this by tilting a glass plate, which overlaps the 468 and 544 nm beams (figure 21). The result of this measurement is shown in figure 24 (full curve).

We compare this result with a simple calculation (broken curve). In this calculation we assume that the applied electric field is a sum of five perfectly coherent monochromatic waves: $E(t, \tau_5) = \sum_{m=1}^{5} \frac{1}{5} \cos[\omega_m(t + \tau_m)]$, where $\tau_1 = \tau_2 = \tau_3 = 0$, $\tau_4 = 0.93\tau_5$ and τ_5 is the variable time delay, which is calculated from the tilt angle of the glass plate. (When we tilt the plate, the time delay for the two beams is not the same, because of dispersion in glass, and also because of the fact that the two beams cross the plate at slightly different angles; the factor 0.93 accounts for this difference.) In our experiments, we have adjusted the intensities such that each frequency component contributes approximately equally to the ion production. Therefore it is reasonable to take the amplitudes of the five terms in the sum as equal. Furthermore, we assume an ideal sixth-order response of the atomic system and calculate the expected ion signal as $\int [E(t, \tau_5)]^{12}\, dt$. We observe a good qualitative agreement of our experimental data with this calculation.

We also perform a more rigorous frequency-domain calculation (dotted curve in figure 24). In this calculation we take experimental values for the sideband energies and assume diffraction-limited focusing for each sideband. We perform a perturbative calculation of ionization probability and include all known Xe energy levels [110] and all possible ionization paths. Since the dipole matrix elements between Xe energy levels are not known, we assume that their relative values are equal. We normalize these matrix elements so that the total oscillator strength from each level to all other levels is approximately equal to unity. We observe a very good agreement between our two calculations (broken and dotted curves in figure 24) and between theory and experiment. In the frequency-domain calculation we also find, in rough agreement with our experimental data (figure 23), that the seventh-order process dominates, while sixth- and eighth-order processes have smaller but comparable contributions to the ionization of Xe.

If all energy levels and matrix elements for Xe were known, then a precise frequency-domain calculation could be accomplished. Difficulties arise because we are trying to proceed without knowing the details of the atomic system. In order to interpret our experimental results it is therefore advantageous to use a combination of the two theoretical approaches:

(1) the simplified time-domain calculation, which makes no assumptions about the atomic system, except for the experimentally measured sixth-order power dependence, and
(2) the more rigorous frequency-domain calculation, which assumes equal matrix elements for all known dipole-allowed transitions.

Fortuitously, the two calculations produce almost identical results.

Another example of a correlation-like trace is shown in figure 25. Here, we measure the ion signal, produced by our five sidebands, as a function of the 544 nm beam phase. Data points, with error bars showing our experimental fluctuations, are fitted by our simple theory (broken curve, $\int [\sum_{m=1}^{5} \cos(\omega_m t + \varphi_m)]^{12}\, dt$, with a variable φ_4). This dependence can be considered as a correlation of two periodic waveforms (with the same period): one synthesized by 544 and 807 nm beams, and the other waveform synthesized by 468 nm, 650 nm and 1.06 μm beams. If we accept this point of view, we can put a timescale on the horizontal axis of figure 25, such that the delay between the two peaks is 5.5 fs (which is the period of the two correlated waveforms) and the peak width roughly equals 2 fs.

9.4.2. Phase adjustment by variable dispersion. To investigate the broadband nature of our waveform and to

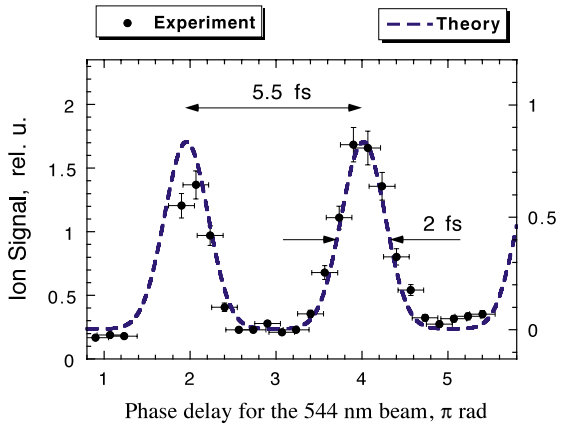

Figure 25. The ion yield as a function of the 544 nm beam phase. This dependence can be considered as a correlation of two waveforms: one synthesized by 544 and 807 nm beams, and the other waveform synthesized by 468, 650 nm and 1.06 μm beams; then, the delay between the two peaks is 5.5 fs (which is the period of the two correlated waveforms), and the peak width roughly equals 2 fs.

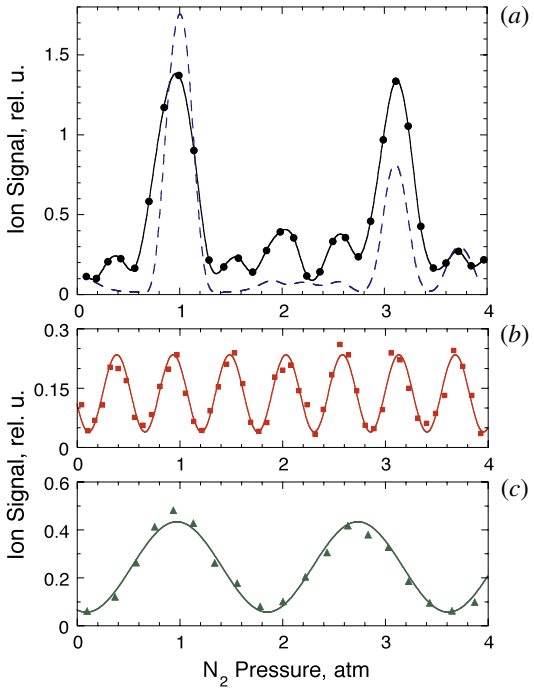

Figure 26. Number of Xe ions produced in the set-up of figure 21, versus pressure in the N_2 cell. For part (*a*) all five sidebands are present. For parts (*b*) and (*c*) we leave only three equidistant sidebands (1.06 μm, 650, 468 nm for part (*b*), and 650, 544, 468 nm for part (*c*)). The full curve is a cubic spline interpolation of the data in part (*a*) and a sinusoidal fit to the data in parts (*b*) and (*c*). The broken curve in part (*a*) is a theoretical calculation. For the data in part (*a*), we observe significant saturation for ion signal above 1 rel u (see text for details) (reprinted from [11]).

further test the mutual coherence among the sidebands, we use variable dispersion. We put a gas cell (34 cm long) into the combined beam (just before the Xe cell, figure 21) and fill it with nitrogen gas (N_2). We adjust sideband phases such that the ion signal maximizes for 1 atm pressure and count the number of Xe ions per laser shot as a function of N_2 pressure (figure 26(*a*)). We observe a sharp decrease in the ion signal as the N_2 pressure changes. This is caused by dispersion in N_2. As the N_2 pressure changes by 2.2 atm, the dispersion is such that the sidebands rephase and the ion signal increases. We repeat this experiment for subsets of three equally spaced sidebands. We observe a nearly sinusoidal dependence of the ion signal on N_2 pressure (figures 26(*b*) and (*c*)). (A related result was obtained by Karapanagioti *et al* [111]. They have demonstrated coherent control in four-photon excitation schemes, using third harmonic together with fundamental laser frequency.) Note that, in our experiment, the higher the frequency separation among these three sidebands, the smaller the change in N_2 pressure is required to produce a π phase shift among them. The broken curve in figure 26(*a*) shows a result of the simple calculation: $\int[\sum \cos(\omega_m t + \varphi_m)]^{12}\,\mathrm{d}t$, where the phases φ_m are determined by N_2 pressure (frequency-dependent refractive index of N_2 is obtained from [112]).

9.5. Prospectives for absolute phase control

It is known that a phase-locked spectrum, with a bandwidth equal to one octave, corresponds to single-cycle pulses. In the past, single-cycle (and sub-cycle) pulses were available only in the THz spectral region, with a duration of about 0.5 ps [113]. The experimental results, presented in this section (in particular, high contrast of the ion signal in figures 22–26 and the theory/experiment agreement) establish evidence for a good mutual coherence among frequency components, which extend over an octave of optical bandwidth, and prove our ability to phase-lock these components. Thus we infer that in this experiment we are able to synthesize trains of single-cycle pulsed waveforms (with a repetition period of 11 fs, a pulse duration of 2 fs and a random absolute phase).

The absolute phase, or the phase of the field oscillation with respect to the pulse envelope, becomes an important parameter even for couple-cycle pulses. Control over the optical phase under the pulse envelope is the first step toward the sub-cycle pulse shaping. The absolute phase phenomena is an emerging field in femtosecond atomic physics. Researchers learn measuring and controlling the absolute phase of few-femtosecond pulses produced by mode-locked lasers [114–117]. For the Raman technique, the absolute phase control can be achieved by using tunable lasers with frequencies equal to a multiple of the molecular modulation frequency. The resultant trains of identical single-cycle pulses can be used to study, for example, the dependence of photoionization on the absolute phase. In such an experiment, the signal from all pulses in the train will add coherently.

In summary, this section shows that our source can be used to study multiphoton ionization in a regime not accessible by other sources. The photoionization depends on the relative phases of the spectral components and provides a tool for measuring ultrashort pulses. From indirect measurements we infer the pulse length, produced in our present experiment, to be approximately 2 fs (less than one optical cycle of the applied infrared lasers).

10. Conclusion

The highlights of the work, described in this tutorial, are:

(1) We have demonstrated a new light source with ultrawide bandwidth, extending from the infrared to the far-ultraviolet. We have characterized this source and have shown that the spectrum consists of collinear, nearly diffraction-limited sidebands, which are mutually coherent across their spatial and temporal profiles, and thus can be used to synthesize an arbitrary desired waveform in a target cell.

(2) We have shown that this source can be used to study multiphoton ionization in a single-cycle regime. We have demonstrated that there is enough energy in the generated beams that sideband phase drifts are not too large to prevent us from adjusting their phases in real time, and that the beam pointing is stable enough to allow tight focusing with a good, and stable from shot to shot, sideband overlap. In this experiment, which became the culmination of this PhD work, we have studied photoionization in a regime not accessible by other techniques and have used the nonlinearity of the ionization process to characterize our light source.

(3) The foundation for these experimental achievements was the understanding of the nature of molecular modulation. Frequency modulation by molecular motion turned out to be an important concept, which allowed extension of our ideas to a wider range of problems. It should be noted that, although any Raman process can be described in terms of molecular modulation, this concept becomes fully valid and useful only in the regime of maximal molecular coherence.

A growing activity in the area of molecular modulation proves the vitality of this new field. Recent experiments have shown that a weak probe pulse can be compressed by molecular oscillations which are excited impulsively by a strong pump pulse [32, 118, 119]. Kalosha *et al* [65] have suggested that molecular wavepacket revivals can produce frequency chirp, which in turn would allow femtosecond pulse compression by normal dispersion in a thin output window. Bartels *et al* [120] have demonstrated this possibility experimentally. Kolesov and Kocharovskaya [121] have proposed to use a CW optical pumping into the coherent superposition state in order to achieve broadband Raman generation in solid-state media. The adiabatic Raman technique has allowed collinear generation of rotational sidebands in H_2 with a 100% conversion efficiency [122]. Shon *et al* [123] have proposed a selective frequency converter with spectral power distribution controlled by applying the driving fields at an angle, in order to allow adjustments of the wavevector of the produced coherence. A multiplicative technique has been proposed for the case where several Raman transitions are excited by applying several frequencies at the input of the medium [124].

There has been a proposal to combine the adiabatic Raman technique with the impulsive technique. According to this method, a short probe pulse can be compressed into a singlet, doublet or triplet of subfemtosecond pulses by beating with an adiabatically prepared Raman coherence [64]. This method has the advantage of the adiabatic pumping in producing a large Raman coherence and the advantage of the impulsive excitation in reducing the number of pulses per train. The proposal relies on a thorough understanding of the mechanisms of molecular modulation [50].

It is useful to put this work in perspective with regard to other ultrafast techniques. According to the Heisenberg uncertainty relationship, access to the ultra-short timescale requires a high energy per particle. The fastest processes in nature occur in high-energy collisions and nuclear reactions. The techniques of high-energy and nuclear physics allow only a theoretical reconstruction of the time-domain evolution of individual events, and do not allow direct observation and control. In contrast, by using optical techniques one can directly record and precisely control ultra-fast fundamental processes in atoms and molecules. Present solid-state laser technology allows coherent control of molecular dynamics and chemical reactions on a timescale approaching a few femtoseconds [4–8]. Electronic motion in atoms occurs on a shorter, subfemtosecond timescale. Subfemtosecond pulses may be used to observe and control rapid motion of inner-shell electrons, or could provide information about fast ionization processes [9].

Femtosecond pulses consist of a few optical cycles and allow synthesis of shaped waveforms with controlled amplitude and frequency. These waveforms are limited to quasi-sinusoidal pulse shapes. A subfemtosecond pulse duration is shorter than a single optical cycle for the visible spectral region. When used for pulse shaping, sub-cycle pulses will provide an unprecedented opportunity to control not just the pulse envelope (amplitude and frequency as functions of time), but also the shape of the electric field itself. We predict the possibility for the synthesis of non-sinusoidal waveforms where the electric field is an arbitrary predetermined function of time. As a result, a direct and precise control of electron trajectories in photoionization and HHG will become possible.

Acknowledgments

Funding and support. This PhD tutorial is adapted from a Dissertation submitted by A V Sokolov to the Department of Physics, Stanford University, in partial fulfillment of the requirements for the PhD degree. This work was supported by the US Office of Naval Research, the US Air Force Office of Scientific Research and the US Army Research Office. A V Sokolov also acknowledges support from Texas Advanced Research Program, and from the Welch Foundation.

A V Sokolov. I would like to thank my Stanford PhD adviser, and co-author of this PhD tutorial, Steve Harris, for the opportunity to work under his guidance and to learn from him. I appreciate every minute of the long hours of our discussions. I truly admire his talents. I want to thank Stanford Professors Tony Siegman, Steve Chu and Bob Byer, who provided me with critical comments on my results over the course of my work. I would also like to thank Professors Yoshi Yamomoto, Mark Kasevich and Marty Fejer, for the knowledge that I have acquired from their courses, and from discussions with them.

I am especially grateful to Guang-Yu Yin; I realize that the success of my experiments would not have been possible without his support. I want to give special thanks to my teammates, and co-authors of most of the work presented in this PhD tutorial, David Walker and Deniz Yavuz. I am grateful to other Harris group members: Maneesh Jain, Andrew Merriam,

Hui Xia, Scott Sharpe, Miroslav Shverdin, Danielle Manuszak and Vlatko Balic. Many ideas were born in discussions, at our group meetings, and in everyday conversations with them. I thank our secretary Sue Dutcher for being supportive, for her affection and good cheer. I would also like to thank my new co-workers at Texas A&M University: Miaochan Zhi, Roman Kolesov, Andrea Burzo and Igor Mariyenko.

I gratefully appreciate support from my good friends and colleagues Vlad Shalaev, Misha Ivanov, Paul Corkum, Alex Gaeta, Misha Lukin, Michael Fleischhauer, Olga Kocharovskaya, Marlan Scully, Ed Fry, George Welch, Pierre Agostini, Kohzo Hakuta, Fam Le Kien, Dmitry Nikonov, Yuri Rostovtsev, Andrey Matsko and many others. I would like to thank my professors from Moscow Institute of Physics and Technology, who taught me the basics of everything a physicist should know, and my former colleagues at the General Physics Institute, in Laser Biophysics Laboratory, headed by Valery Vasil'evich Savransky. In particular, I want to thank my adviser there, Anatoly Anatolievich Spikhalsky. I am grateful to my fellow PhysTechs, everyone I studied with in Moscow, and many that I met later, for their continuing support and friendship. I am grateful to all my friends in US, Russia and Ukraine for being with me and supporting me constantly. Finally, I want to thank my family in Ukraine. I feel their support always.

References

[1] Corkum P 1995 *Opt. Photonics News* **6** 18
[2] Krausz F, Brabec T, Schnurer M and Spielmann C 1998 *Opt. Photonics News* **9** 46
[3] Brabec T and Krausz F 2000 *Rev. Mod. Phys.* **72** 545
[4] Zewail A 2000 *J. Phys. Chem.* A **104** 5660
[5] Rice S A and Zhao M 2000 *Optical Control of Molecular Dynamics* (New York: Wiley)
[6] Shapiro M and Brumer P 2000 *Adv. At. Mol. Opt. Phys.* **42** 287
[7] Warren W S, Rabitz H and Dahleh M 1993 *Science* **259** 1581
[8] Levis R J and Rabitz H A 2002 *J. Phys. Chem.* A **106** 6427
[9] Krausz F 2001 *Phys. World* **14** 41
[10] Sokolov A V, Walker D R, Yavuz D D, Yin G Y and Harris S E 2000 *Phys. Rev. Lett.* **85** 562
[11] Sokolov A V, Walker D R, Yavuz D D, Yin G Y and Harris S E 2001 *Phys. Rev. Lett.* **87** 033402
[12] Fork R L, Brito-Cruz C H, Becker P C and Shank C V 1987 *Opt. Lett.* **12** 483
[13] Baltuška A, Wei Z, Pshenichnikov M S and Wiersman D A 1997 *Opt. Lett.* **22** 102
[14] Nisoli M, DeSilvestri S, Svelto O, Szipocs R, Ferencz K, Spielmann Ch, Sartania S and Krausz F 1997 *Opt. Lett.* **22** 522
[15] Steinmeyer G, Sutter D H, Gallmann L, Matuschek N and Keller U 1999 *Science* **286** 1507
[16] Hansch T W 1990 *Opt. Commun.* **80** 71
[17] Farcas Gy and Toth Cs 1992 *Phys. Lett.* A **168** 447
[18] Harris S E, Macklin J J and Hansch T W 1993 *Opt. Commun.* **100** 487
[19] Antoine P, 'Huiller A L and Lewenstein M 1996 *Phys. Rev. Lett.* **77** 1234
[20] Schafer K J and Kulander K C 1997 *Phys. Rev. Lett.* **78** 638
[21] Corkum P B, Burnett N H and Ivanov M Y 1994 *Opt. Lett.* **19** 1870
[22] Christov I P, Murnane M M and Kapteyn H C 1997 *Phys. Rev. Lett.* **78** 1251
[23] Yoshikawa S and Imasaka T 1993 *Opt. Commun.* **96** 94
[24] Kawano H, Hirakawa Y and Imasaka T 1998 *IEEE J. Quantum Electron.* **34** 260
[25] Kaplan A E 1994 *Phys. Rev. Lett.* **73** 1243
[26] Kaplan A E and Shkolnikov P L 1996 *J. Opt. Soc. Am.* B **13** 347
[27] Belenov E M, Nazarkin A V and Prokopovich I P 1992 *Pis. Zh. Eksp. Teor. Fiz.* **55** 223
[28] Belenov E M, Kryukov P G, Nazarkin A V and Prokopovich I P 1994 *Zh. Eksp. Teor. Fiz.* **105** 28
[29] Prokopovich I P and Khrushckinskii A A 1997 *Laser Phys.* **7** 305
[30] Kaplan A E and Shkolnikov P L 1995 *Phys. Rev. Lett.* **75** 2316
[31] Kalosha V P and Herman J 1999 *Phys. Rev. Lett.* **83** 544
[32] Zhavoronkov N and Korn G 2002 *Phys. Rev. Lett.* **88** 203901
[33] Drescher M, Hentschel M, Kienberger R, Tempea G, Spielmann Ch, Reider G A, Corkum P B and Krausz F 2001 *Science* **291** 1923
[34] Paul P M, Toma E S, Breger P, Mullot G, Auge F Balcou Ph, Muller H G and Agostini P 2001 *Science* **292** 1689
[35] Hentschel M, Kienberger R, Spielmann Ch, Reider G A, Milosevic N, Brabec T, Corkum P, Heinzmann U, Drescher M and Krausz F 2001 *Nature* **414** 509
[36] Harris S E and Sokolov A V 1997 *Phys. Rev.* A **55** R4019
[37] Harris S E and Sokolov A V 1998 *Phys. Rev. Lett.* **81** 2894
[38] Sokolov A V, Yavuz D D and Harris S E 1999 *Opt. Lett.* **24** 557
[39] Sokolov A V 1999 *Opt. Lett.* **24** 1248
[40] Sokolov A V, Yavuz D D, Walker D R, Yin G Y and Harris S E 2001 *Phys. Rev.* A **63** 051801
[41] Harris S E 1994 *Opt. Lett.* **19** 2018
[42] Yavuz D D, Sokolov A V and Harris S E 2000 *Phys. Rev. Lett.* **84** 75
[43] Harris S E 1997 *Phys. Today* **50** 36
[44] Scully M O and Zubairy M. S 1997 *Quantum Optics* (Cambridge: Cambridge University Press)
[45] Jain M, Xia H, Yin G Y, Merriam A J and Harris S E 1996 *Phys. Rev. Lett.* **77** 4326
[46] Sokolov A V, Sharpe S, Shverdin M, Walker D R, Yavuz D D, Yin G Y and Harris S E 2001 *Opt. Lett.* **26** 728
[47] Hillegas C W, Tull J X, Goswami D, Strickland D and Warren W S 1994 *Opt. Lett.* **19** 737
[48] Weiner A M 1995 *Prog. Quantum Electron.* **19** 161
[49] Baumert T, Brixner T, Seyfried V, Strehle M and Gerber G 1997 *Appl. Phys.* B **65** 779
[50] Kien Fam Le, Hakuta K and Sokolov A V 2002 *Phys. Rev.* A **66** 023813
[51] Allen L and Eberly J H 1987 *Optical Resonance and Two-Level Atoms* (New York: Dover) p 75
[52] Kocharovskaya O and Mandel P 1990 *Phys. Rev.* A **42** 523
[53] Scully M O 1991 *Phys. Rev. Lett.* **67** 1855
[54] Hakuta K, Marmet L and Stoicheff B P 1991 *Phys. Rev. Lett.* **66** 596
[55] Agarwal G S 1993 *Phys. Rev. Lett.* **71** 1351
[56] Grobe R, Hioe F T and Eberly J H 1994 *Phys. Rev. Lett.* **73** 3183
[57] Jain M, Merriam A J, Kasapi A, Yin G Y and Harris S E 1995 *Phys. Rev. Lett.* **75** 4385
[58] Gaubatz U, Rudecki P, Becker M, Schiemann S, Külz M and Bergmann K 1988 *Chem. Phys. Lett.* **149** 463
[59] Grischkowsky D 1970 *Phys. Rev. Lett.* **24** 866
[60] Grischkowsky D and Armstrong J A 1972 *Phys. Rev.* A **6** 1566
[61] Grischkowsky D, Loy M M T and Liao P F 1975 *Phys. Rev.* A **12** 2514
[62] Oreg J, Hioe F T and Eberly J H 1984 *Phys. Rev.* A **29** 690
[63] Kalosha V P and Herrmann J 2000 *Phys. Rev. Lett.* **85** 1226
[64] Kien Fam Le, Shon Nguyen Hong and Hakuta K 2001 *Phys. Rev.* A **64** 051803(R)
[65] Kalosha V, Spanner M, Herrmann J and Ivanov M 2002 *Phys. Rev. Lett.* **88** 103901
[66] Kien Fam Le, Hakuta K and Sokolov A V 2002 Frequency modulation and pulse compression by coherent multimode molecular motion *Phys. Rev.* A at press

[67] Kocharovskaya O A, Khanin Ya I and Tsaregradskii V B 1986 *Sov. J. Quantum Electron.* **16** 127
[68] Kien F L, Liang J Q, Katsuragawa M, Ohtsuki K, Hakuta K and Sokolov A V 1999 *Phys. Rev.* A **60** 1562
[69] Allison A C and Dalgarno A 1970 *At. Data* **1** 289
[70] Herzberg G 1950 *Molecular Spectra and Molecular Structure: I. Spectra of Diatomic Molecules* (New York: Van Nostrand-Reinhold)
[71] Demers J R and DeLucia F C 1999 *Opt. Lett.* **24** 250
[72] Ramaswamy-Paye M and Fujimoto J G 1994 *Opt. Lett.* **19** 1756
[73] Bouma B E and Fujimoto J G 1996 *Opt. Lett.* **21** 134
[74] Xu L, Tempea G, Spielmann Ch, Krausz F, Stingl A, Ferencz K and Takano S 1998 *Opt. Lett.* **23** 789
[75] Beddard T, Sibbett W, Reid D T, Garduno-Mejia J, Jamasbi N and Mohebi M 1999 *Opt. Lett.* **24** 163
[76] Zhou J, Taft G, Huang C-P, Murnane M M, Kapteyn H C and Christov I P 1994 *Opt. Lett.* **19** 1149
[77] Stingl A, Lenzner M, Spielmann Ch, Krausz F and Szipocz R 1995 *Opt. Lett.* **20** 602
[78] Kasper A and Witte K J 1996 *Opt. Lett.* **21** 360
[79] Hakuta K, Suzuki M, Katsuragawa M and Li J Z 1997 *Phys. Rev. Lett.* **79** 209
[80] Li J Z, Katsuragawa M, Suzuki M and Hakuta K 1998 *Phys. Rev.* A **58** R58
[81] Dicke R H 1953 *Phys. Rev.* **89** 472
[82] Hagenlocker E E, Minck R W and Rado W G 1967 *Phys. Rev.* **154** 226
[83] Owyoung A 1978 *Opt. Lett.* **2** 91
[84] Konovalov I G, Morozov V B, Tunkin V G and Mikheev A V 1995 *J. Mol. Struct.* **348** 41
[85] Udem Th, Reichert J, Holzwarth R and Hansch T W 1999 *Phys. Rev. Lett.* **82** 3568
[86] Schulz-von der Gathen V, Bornemann T, Kornas V and Dobele H F 1990 *IEEE J. Quantum Electron.* **26** 739
[87] Losev L L and Lutsenko A P 1993 *Quantum Electron.* **23** 919
[88] McDonald G S, New G H C, Losev L L, Lutsenko A P and Shaw M 1994 *Opt. Lett.* **19** 1400
[89] Liang J Q, Katsuragawa M, Kien Fam Le and Hakuta K 2000 *Phys. Rev. Lett.* **85** 2474
[90] Nazarkin A, Korn G, Wittman M and Elsaesser T 1999 *Phys. Rev. Lett.* **83** 2560
[91] Ruhman S, Joly A G and Nelson K A 1988 *IEEE J. Quantum Electron.* **24** 460
[92] Kasapi A, Jain M and Yin G Y 1996 *Appl. Phys. Lett.* **35** 1999–2022
[93] Siegman A E 1986 *Lasers* (Mill Valley, CA: University Science)
[94] Russel D A and Roh W B 1987 *J. Mol. Spectrosc.* **124** 240
[95] Lucht R P and Farrow R L 1988 *J. Opt. Soc. Am.* B **5** 1243
[96] Bergmann K, Theuer H and Shore B W 1998 *Rev. Mod. Phys.* **70** 1003
[97] Shen Y R 1984 *The Principles of Nonlinear Optics* (New York: Wiley)
[98] Yariv A 1989 *Quantum Electronics* 3rd edn (New York: Wiley)
[99] Merriam A J, Sharpe S J, Xia H, Manuszak D, Yin G Y and Harris S E 1999 *Opt. Lett.* **24** 625
[100] Holmes R and Flusberg A 1988 *Phys. Rev.* A **37** 1588
[101] Villeneuve D M, Aseyev S A, Dietrich P, Spanner M, Ivanov M Yu and Corkum P B 2000 *Phys. Rev. Lett.* **85** 542
[102] Oudar J-L and Shen Y R 1980 *Phys. Rev.* A **22** 1141
[103] Begley R F, Harvey A B and Byer R L 1974 *Appl. Phys. Lett.* **25** 337
[104] Frey R, Pradere F and Ducuing J 1976 *Opt. Commun.* **18** 2045
[105] Loy M M T, Sorokin P P and Lankard J R 1977 *Appl. Phys. Lett.* **30** 415
[106] Laubereau A, Wochner G and Kaiser W 1976 *Phys. Rev.* A **13** 2212
[107] Frey R, Pradere F, Lukasik J and Ducuing J 1977 *Opt. Commun.* **22** 355
[108] Sorokin P P, Wynne J J and Lankard J R 1973 *Appl. Phys. Lett.* **22** 342
[109] Bethune D S, Lankard J R and Sorokin P P 1979 *Opt. Lett.* **4** 103
[110] Moore C E 1971 *Atomic Energy Levels* NSRDS-NBS Circular no 35, vol 3 (Washington, DC: US Government Printing Office)
[111] Karapanagioti N E, Xenakis D, Charalambidis D and Fotakis C 1996 *J. Phys. B: At. Mol. Opt. Phys.* **29** 3599
[112] Craven E C 1945 *Proc. Phys. Soc.* **57** 97
[113] Jones R R, You D and Bucksbaum P H 1993 *Phys. Rev. Lett.* **70** 1236
[114] Apolonski A, Poppe A, Tempea G, Spielmann Ch, Udem Th, Holzwarth R, Hansch T W and Krausz F 2000 *Phys. Rev. Lett.* **85** 740
[115] Telle H R, Steinmeyer G, Dunlop A E, Stenger J, Sutter D H and Keller U 1999 *Appl. Phys.* B **69** 327–32
[116] Jones D J, Diddams S A, Ranka J K, Stentz A, Windeler R S, Hall J L and Cundiff S T 2000 *Science* **288** 635
[117] Paulus G G, Grasbon F, Walther H, Villoresi P, Nisoli M, Stagira S, Priori E and DeSilvestri S 2001 *Nature* **414** 182
[118] Wittman M, Nazarkin A and Korn G 2000 *Phys. Rev. Lett.* **84** 5508
[119] Wittman M, Nazarkin A and Korn G 2001 *Opt. Lett.* **26** 298
[120] Bartels R A, Weinacht T C, Wagner N, Baertschy M, Greene C H, Murnane M M and Kapteyn H C 2002 *Phys. Rev. Lett.* **88** 013903
[121] Kolesov R 2001 *Phys. Rev.* A **64** 063819
[122] Yavuz D D, Walker D R, Yin G Y and Harris S E 2002 *Opt. Lett.* **27** 769
[123] Shon Nguyen Hong, Kien Fam Le, Hakuta K and Sokolov A V 2002 *Phys. Rev.* A **65** 033809
[124] Harris S E, Walker D R and Yavuz D D 2002 *Phys. Rev.* A **65** 021801